Seismic Velocity Structure Along and Across the Ultraslow-Spreading Southwest Indian Ridge at 64°30'E Showcases Flipping Detachment Faults

A. Corbalán, M. Nedimović, K. Louden, M. Cannat, I. Grevemeyer, L. Watremez, Sylvie Leroy

Seismic Velocity Structure Along and Across the Ultraslow-Spreading Southwest Indian Ridge at 64°30'E Showcases Flipping Detachment Faults

A. Corbalán[1,*], M.R. Nedimović[1], K.E. Louden[2], M. Cannat[3], I. Grevemeyer[4], L. Watremez[5], and S. Leroy[6]

[1]Department of Earth and Environmental Sciences, Dalhousie University, Halifax, NS, Canada.

[2]Department of Oceanography, Dalhousie University, Halifax, NS, Canada.

[3]Geoscience Marines, Université de Paris, Institut de Physique du Globe de Paris, UMR 7154 CNRS, Paris, France.

[4]GEOMAR Helmholtz Centre for Ocean Research, Kiel, Germany.

[5]Laboratoire d'Océanologie et de Géosciences, Université Lille, CNRS, Université Littoral Côte d'Opale, Lille, France.

[6]Sorbonne Université, CNRS-INSU, Institut des Sciences de la Terre de Paris, ISTeP, France.

[*]Corresponding author: Ana Corbalán (a.corbalan@dal.ca)

Key Points:

- First detailed 2D regional P-wave velocity models across and along an ultraslow-spreading Southwest Indian Ridge amagmatic segment
- A system of flipping detachments is imaged in the subsurface for the first time constrained by the velocity structure
- Lithosphere gradually transitions from highly fractured and fully serpentinized peridotites at the top to unaltered peridotites at depth

Abstract

We present two ~150-km-long orthogonal 2-D P-wave tomographic velocity models across and along the ridge axis of the ultraslow-spreading Southwest Indian Ridge at 64°30'E. Here, detachment faults largely accommodate seafloor accretion by mantle exhumation. The velocity models are constructed by inverting first arrival traveltimes recorded by 32 ocean bottom seismometers placed on the two profiles. The velocities increase rapidly with depth, from 3–3.5 km/s at the seafloor to 7 km/s at depths ranging from 1.5–6 km below the seafloor. The vertical gradient decreases for velocities >7 km/s. We suggest that changes in velocity with depth are related to changes in the degree of serpentinization and interpret the lithosphere to be composed of highly fractured and fully serpentinized peridotites at the top with a gradual downward decrease in serpentinization and pore space to unaltered peridotites. One active and five abandoned detachment faults are identified on the ridge-perpendicular profile. The active axial detachment fault (*D1*) shows the sharpest lateral change (horizontal gradient of ~1 s^{-1}) and highest vertical gradient (~2 s^{-1}) in the velocities. In the western section of the ridge-parallel profile, the lithosphere transitions from non-volcanic to volcanic over a distance of ~10 km. The depth extent of serpentinization on the ridge-perpendicular profile ranges from ~2-5 km, with the deepest penetration at the *D1* hanging wall. On the ridge-parallel profile, this depth (~2.5-4 km) varies less as the profile crosses the *D1* hanging wall at ~5-9 km south of the ridge axis.

Plain Language Summary

We investigate the Southwest Indian Ridge lithosphere at 64°30'E, where the Somalian and Antarctic plates move slowly away from each other at less than 14 mm/year. This is one of a limited number of places on Earth where mantle is currently being exhumed to the seafloor. We use seismic sensors, placed across and along the ridge axis, to analyze how seismic waves travel from the energy sources, through the lithosphere, to these sensors. Our results, in the form of two-dimensional velocity models, show that the rock velocities increase rapidly with depth. Lateral and vertical velocity changes delimit a system of detachment faults on the ridge-perpendicular profile, responsible for bringing mantle-derived rocks, peridotites, up to the seafloor. Based on the modeled velocities and velocity changes, and previous extensive seafloor sampling, we suggest that ~75% of the lithosphere in the study area is composed of highly fractured and fully hydrothermally altered peridotites at the top with a gradual downward decrease in alteration and pore space to unaltered peridotites at depth. We also locate the transition to lithosphere with a magmatic component in the western section of the ridge-parallel profile.

1 Introduction

The global mid-ocean ridge system consists of spreading centres that greatly differ from each other in their spreading rate, spreading obliquity, melt supply and modes of seafloor accretion. Oceanic ridges are normally classified by their full-spreading rate as fast- (~80–180 mm/yr), intermediate- (~55–70 mm/yr), slow- (20-55mm/yr), and ultraslow-spreading (<~20 mm/yr) (Dick et al., 2003). The scientific community has invested significant effort into studying the oceanic crust formed at fast- (e.g. Aghaei et al., 2014; Canales et al., 2003; Detrick et al., 1993; Dunn & Toomey, 2001; Grevemeyer et al., 1998; Han et al., 2014; Vera & Diebold, 1994), intermediate- (e.g. Canales et al., 2005; Carbotte et al., 2006, 2008; Nedimović et al., 2005, 2008; Newman et al., 2011; Weekly et al., 2014) and slow-spreading rates (e.g. Arnulf et al.,

2012; Barclay et al., 1998; Christeson et al., 2020; Dannowski et al., 2010; Escartín & Canales, 2011; Estep et al., 2019; Kardell et al., 2019; Seher et al., 2010, Xu et al., 2020). Less effort has been directed toward studying the lithosphere formed at ultraslow-spreading ridges, which thus remains relatively less well understood. Yet, the ultraslow-spreading centers constitute about 35% of the global ridge system (Dick et al., 2003). The comparatively smaller effort put toward understanding the lithosphere at ultra-slow ridges is partially a consequence of their remoteness and inaccessibility, as these ridges are located in the Arctic (Gakkel Ridge, Knipovich Ridge, Mohns Ridge, and Kolbeinsey Ridge) and Indian Oceans (Southwest Indian Ridge - SWIR) (Argus et al., 2011; Bird, 2003; Kreemer et al., 2014; Müller et al., 2008).

Early controlled-source seismic surveys (e.g. Ewing & Ewing, 1959; Houtz & Ewing, 1976; Peterson et al., 1974; Raitt, 1963; Talwani et al., 1965, 1971), in situ rock investigations and laboratory velocity measurements on rock samples (e.g. Carlson & Miller, 1997, 2003; Christensen, 1972; Christensen & Salisbury, 1975; Miller & Christensen, 1997), and ophiolite studies (e.g. Christensen, 1978; Christensen & Smewing, 1981) suggest an oceanic crustal structure composed of three seismically identifiable layers that often correspond, from top to bottom, to an extrusive basaltic lava layer (Layer 2A), a sheeted diabase dike layer (Layer 2B), and a Layer 3 comprised of isotropic gabbros at the top and layered gabbros at the bottom topping the uppermost mantle. However, the seismic boundaries do not necessarily correspond to lithological boundaries. For instance, the layer 2A/2B boundary, which is thought to be an alteration front or a major change in porosity, may or may not correspond to a change in lithology (e.g. Berge et al., 1992; Carbotte and Scheirer, 2004; Christeson et al., 2007; Wilcock et al., 1992). Igneous mafic layers 2A, 2B and 3 are often distinguished according to their commonly associated velocity and thickness ranges, as well as their vertical velocity gradients (Christeson et al., 2019; Grevemeyer et al., 2018a; White et al., 1992). However, identified outcrops of exposed mantle-derived peridotites on the seafloor at slow- and ultraslow-spreading ridges (e.g. Blackman et al., 2002; Cannat et al., 2006; Dick et al., 2008; Ildefonse et al., 2007) have challenged the 3-layer paradigm at slower spreading rates. Moreover, sampling of the seafloor at the SWIR has nearly exclusively (~90%) recovered serpentinized peridotites (Sauter et al., 2013) suggesting the total absence of continuous igneous mafic layers at the sampled locations.

Exhumed mantle seafloor exposures are generally associated with detachment faults (e.g. Canales et al., 2004; Cannat, 1993; Sauter et al., 2013; Tucholke & Lin, 1994) and Oceanic Core Complexes (OCCs) at slow- and ultraslow-spreading ridges (e.g. Dick et al., 2019; Escartín et al., 2003; Sauter et al., 2013; Smith et al., 2006; Zhao et al., 2013; Zhou & Dick, 2013). Widespread detachment faulting indeed plays a central role in oceanic lithosphere accretion and plate divergence accommodation at melt-poor ridge sections of slow- and ultraslow-spreading ridges (Cann et al., 1997; Cannat et al., 2006; Escartín et al., 2008; Sauter et al., 2013; Smith et al., 2006), particularly at segment ends as magma is focused toward the segment centers (Lin et al., 1990) and thus is scarce at the ends. At the slow-spreading Mid-Atlantic Ridge (MAR), the mode of asymmetrical accretion along detachment faults can last for 1–3 Myr (Tucholke et al., 1998) while at the SWIR continuous exhumation of mantle-derived rocks has been occurring during the last ~11 Myr in a flip-flop detachment faulting mode (Sauter et al., 2013). Steep long-offset normal faults rotate and flatten as footwall flexural bending occurs exposing the ultramafic mantle peridotites on the detachment surface (deMartin et al., 2007; Dick et al., 2010; Escartín et al., 2003; Ildefonse et al., 2007; Smith et al., 2006; Tucholke et al., 1998). These long-offset

normal faults root on a steeply dipping (~70°) interface (deMartin et al., 2007; Parnell-Turner et al., 2017) at depths up to 20 km (Bickert et al., 2020; Schlindwein & Schmid, 2016).

The exhumed peridotites become hydrothermally altered when in contact with seawater. Peridotite-seawater interactions release large amounts of methane and hydrogen to the water column (Alt et al., 2009; Mével, 2003) making serpentinization relevant to the emergence and thriving of unique microbial communities (e.g. Früh-Green et al., 2018; Kelley et al., 2005; Schrenk et al., 2004). Serpentinization also plays a crucial role in the detachment faulting and favors the development of large-offset low-angle detachment faults (Ildefonse et al., 2007; Lavier et al., 1999; Tucholke et al., 1998). New steep normal faults may initiate and become the new master detachment faults with the same or reverse polarity (e.g. Reston & McDermott, 2011; Sauter et al., 2013). Successive detachment faults that change polarity develop a flip-flop fault mode (Bickert et al., 2020; Reston, 2018; Sauter et al., 2013) and reveal exhumed mantle domains in this process on both sides of the spreading axis (Cannat et al., 2019; Reston, 2018; Sauter et al., 2013). What causes the abandonment of a fault and the initiation of a new master fault with opposite polarity is still under debate.

Coincident multichannel seismic (MCS) reflection and wide-angle ocean bottom seismometer (OBS) refraction surveys at ultraslow-spreading ridges are critical to understanding the crustal and uppermost mantle structure, the faulting dynamics associated with divergence, and the mechanisms of seafloor accretion. Seismic surveys at ultraslow-spreading ridges beyond the SWIR include work done at the Knipovich (Kandilarov et al., 2008, 2010), Mohns (Klingelhöfer et al., 2000), Gakkel (Jokat & Schmidt-Aursch, 2007), and Mid-Cayman (Van Avendonk et al., 2017; Grevemeyer et al., 2018b) spreading centers. At the SWIR, large efforts have been focused on the Dragon Flag OCC at 49°39’E (e.g. Zhao et al., 2013), the anomalously thick magmatic crust inferred at 50°28’E (e.g. Jian et al., 2017; Li et al., 2015), the Atlantis II Fracture Zone at 57°E (e.g. Muller et al., 1997, 2000), the non-volcanic seafloor exposures at 64°30'E (e.g. Momoh et al., 2017), and the mafic crustal structure at 66°E (e.g. Minshull et al., 2006).

In the Fall of 2014, French and Canadian scientists collaborated on the marine geophysical project SISMO-SMOOTH (Leroy & Cannat, 2014) aboard the R/V Marion-Dufresne to carry out a major 2D and 3D MCS and OBS survey across the SWIR at 64°30'E (Fig. 1), one of the geologically most sampled areas of the ultra-slow spreading seafloor. This location was also selected because, albeit remote, it does not have ice floes like the ridges in the Arctic Ocean, which allows for low-risk use of long MCS streamers and large groups of OBSs. The main goal of the SISMO-SMOOTH project was to determine the seismic reflection and velocity structure of an ultraslow-spreading ridge to investigate the geophysical fingerprints of variably serpentinized mantle peridotites, map the lithospheric fabric, and better understand the mantle exhumation dynamics, all in an area where the mode of oceanic lithosphere accretion has been interpreted to form broad exposures of exhumed mantle (Cannat et al., 2006). The first results from the analysis of the collected data were focused on the 2D and 3D MCS reflection imaging (Momoh et al., 2017, 2020). Here, we present the results from a tomographic analysis of two orthogonal ~150-km-long OBS profiles, the north-south (NS) profile that is perpendicular to the spreading axis (SMOO33; Figs. 1a and 1c) and the east-west (EW) that is subparallel to it (SMOO35; Figs. 1a and 1b). The seismic velocity structure imaged along these two profiles provides new information on the subsurface expression of the detachment fault system, including the distribution of the detachment faults, the degree of exhumed mantle serpentinization and its

anisotropy, and the east-west transition from predominantly exhumed mantle to more magma-rich lithosphere.

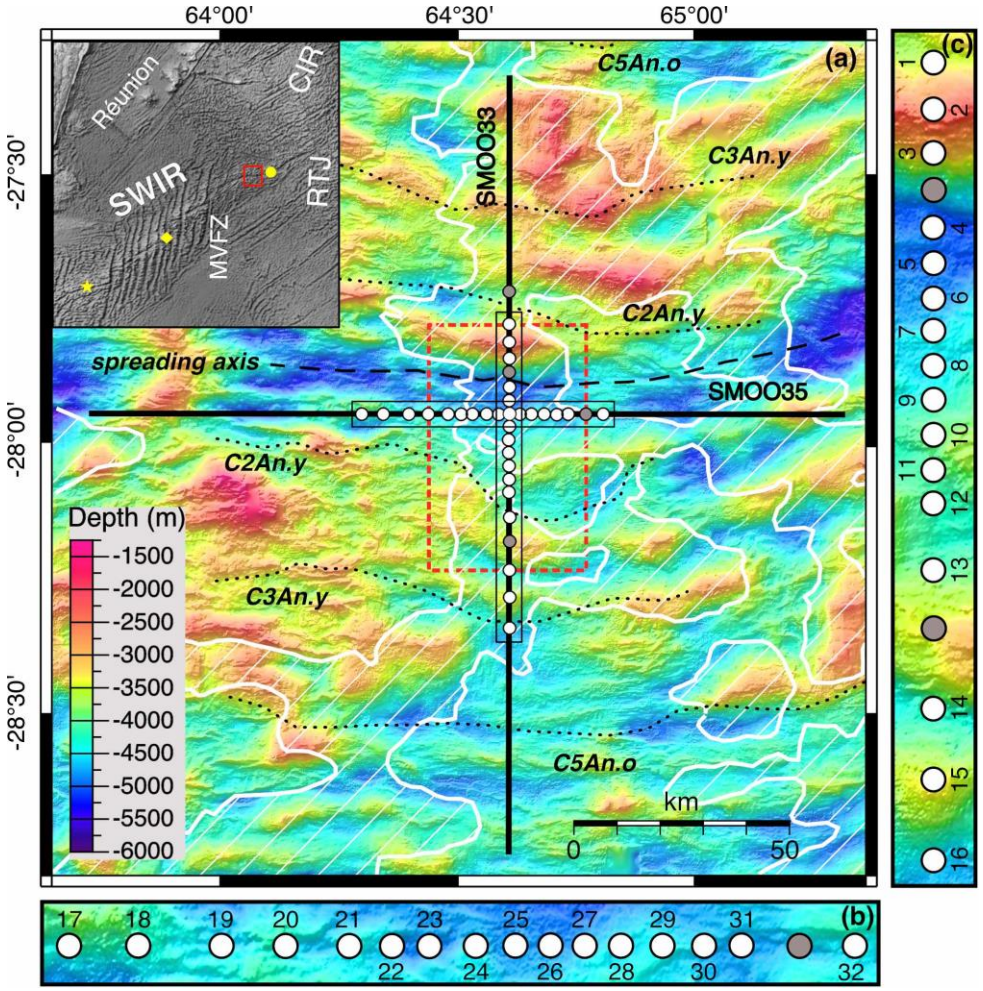

Figure 1. (a) Two regional orthogonal OBS profiles NS (SMOO33) and EW (SMOO35) from the SISMOSMOOTH Survey (Leroy et al., 2015) overlay a bathymetry map (color background; Cannat et al., 2006; Momoh et al., 2017). Thick black lines outline shot locations, and white and gray circles with black outlines are the positions of OBS instruments that did and did not provide useful data, respectively. The shooting distance inside the dashed red rectangle is 150 m and outside 300 m. Dashed black line shows the spreading axis location. Dotted black lines indicate the magnetic anomalies isochrons C2An.y (2.581 Ma), C3An.y (5.894 Ma), and C5An.o (10.949 Ma) (Cande & Kent, 1995; Cannat et al., 2006; Sauter et al., 2008; Reston, 2018). Areas filled with inclined thin white lines and bounded by thick white lines delimit the smooth non-volcanic seafloor (Cannat et al., 2019). Inset in the top left shows the location of the Southwest Indian Ridge (SWIR) relative to the Réunion Island, the Central Indian Ridge (CIR), the Melville Fracture Zone (MVFZ), and the Rodriguez Triple Junction (RTJ). Red rectangle shows the limits of the study area presented in the main figure. The yellow star, diamond and circle indicate the locations of earlier SWIR investigations at 50°E, 57°E and 66°E, respectively. (b, c) Magnifications of the main map within thin black rectangles show positions of the OBS

instruments along the EW (b) and NS (c) profiles. Only the OBS with useful data are sequentially numbered, first in NS and then EW direction.

2 Study area

The SWIR is an ultraslow-spreading center (Dick et al., 2003; Sauter & Cannat, 2010) with a full spreading rate of <14 mm/year (Kreemer et al., 2014). Variations in melt-supply, mantle thermal and compositional heterogeneities, and changes in spreading obliquity along this ridge result in significant large-scale variations of the accreted lithosphere (Cannat et al., 2008). For instance, the easternmost SWIR, east of the Melville Fracture Zone (61°E) and west of the Rodriguez Triple Junction (70°E), is considered to be an endmember in the global ridge system where the interplay between plate- and mantle-driven processes results in a thin or absent mafic igneous crust with a complex relationship between intermittent volcanic edifices, corrugated volcanic seafloor and extensive exhumed mantle domains (Cannat et al., 2003, 2006). At 66°E the mafic igneous crust is estimated to be 2.2-5.4 km thick (Minshull et al., 2006), less than the global average of ~6 km (Chen, 1992; Christeson et al., 2019), while the SWIR at 50°28'E shows an anomalously thick (~9.5 km) crust (Jian et al., 2016). At 64°30'E, which is at the center of our study area (Fig. 1), the SWIR exhibits the widest non-volcanic seafloor documented thus far (Cannat et al., 2006) with on-axis volcanic centres inferred to the east and west (Cannat et al., 2003; Schlindwein & Schmid, 2016).

In the last two decades, several surveys have focused on studying the SWIR at 64°30'E and have used gravity (Cannat et al., 2006), magnetics (Sauter et al., 2008) and side-scan sonar (Sauter et al., 2013) to identify and map the extension of these non-volcanic seafloor domains (Fig. 1a) known as “smooth-seafloor” (Cannat et al., 2006). Variably serpentinized mantle-derived rocks, peridotites, are the dominant lithology at the “smooth-seafloor” (Sauter et al., 2013) and coincide with high residual mantle Bouguer gravity anomaly (RMBA; 30–50 mGal) (Cannat et al., 2006). The seafloor topography is characterized by rounded broad ridges with a height ranging from 500 to 2000 m and a length ranging from 15 to 90 km (Cannat et al., 2006, 2019). Sixteen dredges collected across-axis in the amagmatic corridor of the SWIR at 64°30'E nearly exclusively recovered variably serpentinized peridotites with a minor amount (<5%) of basalts and gabbros (Sauter et al., 2013). Oxygen isotope analyses on these samples suggest relatively high serpentinization temperatures (271–366°C) and in-situ and bulk-rock analyses of the samples support seawater as the serpentinizing fluid, ruling out leaching of basalts or gabbros (Rouméjon et al., 2014). Moreover, the scarcity of melt products is expected as a result of the very low melt supply inferred in the area based on large axial depth and high mean basalt sodium content (Cannat et al., 2008; Meyzen et al., 2003; Seyler et al., 2003).

Momoh et al. (2017) studied the 3D seismic reflection structure at the SWIR at 64°30'E and suggested that the uppermost lithosphere consists of a 4–5 km thick layer mostly composed of serpentinized peridotites with a small proportion of igneous rocks derived from occasional and incipient magmatism. Two main packages of seismic reflectors are imaged across the ridge axis: (1) a group of subparallel reflectors dipping south at 50–60° in the footwall and (2) a group of north dipping reflectors in the hanging wall of the active detachment fault (Momoh et al., 2017). The former are interpreted to be related to the damage zone of the active axial fault, and the latter are suggested to represent either the damage zone of a previously active fault’s footwall or to be related to recent tectonic extension occurring on the hanging wall. Similarly, Momoh et al. (2020) proposed that the crustal-type seismic velocities are related to extensive tectonic damage

and hydrothermal alteration of both peridotites and occasional intruding gabbros. Serpentinization and incipient magmatism are thought to occur in two successive phases: first when mantle-rocks are exhumed on the active detachment fault footwall and later when these rocks constitute the hanging wall of the next detachment fault (Cannat et al., 2019; Momoh et al., 2020).

Microseismicity studies have constrained a thick (20–25 km) brittle lithosphere in the vicinity of our study area (Schlindwein & Schmid, 2016). As a consequence of the virtually-zero melt supply, the seafloor is largely created by successive, flipping polarity, detachment faults that form broad unroofed mantle domains both north and south of the spreading axis (Cannat et al., 2006, 2019; Sauter et al., 2013; Reston, 2018). Active and abandoned detachment fault surfaces have been imaged with side-scan sonar at the SWIR at 64°30'E (Sauter et al., 2013) and seismic reflectors associated with the currently active axial detachment fault have been observed in 3D MCS data (Momoh et al., 2017). Numerical models have demonstrated that a combination of serpentinization and grain size reduction in thick brittle lithosphere can generate flip-flop detachment faulting (Bickert et al., 2020). Detailed bathymetric and kinematic analysis have been carried out to investigate the emergence and breakaway of the interpreted faults and explain the mantle exhumation dynamics at detachment-dominated spreading ridges (Cannat et al., 2019; Reston, 2018). Still lacking, however, is a well-resolved regional-scale velocity model capturing these detachment faults, active and abandoned, to back up or rebut the proposed lithospheric accretion models.

3 Data acquisition and analysis

3.1 Seismic experiment

The MD 199 - SISMO-SMOOTH Cruise 2014 (Leroy & Cannat, 2014; Leroy et al., 2015) in the easternmost SWIR collected a variety of datasets including pseudo-3D MCS (Momoh et al., 2017), 2D MCS (Momoh et al., 2020), 3D wide-angle OBS, and 2D wide-angle OBS. The 3D MCS and 3D OBS data are focused in narrow (1.8x24 km and 20x30 km, respectively) rectangles at the ridge axis, while the 2D profiles extend ~150 km across and along the spreading axis. In this paper, we show and interpret the results from analysis of the regional 2D OBS wide-angle data set (Fig. 1). Shots for the 3D MCS survey recorded by OBSs 4-13 on the NS profile (Fig. 1) were used by Momoh et al. (2017) to form a simple velocity model for migration of the reflection signal. However, none of the regional 2D OBS shots recorded by the 32 OBSs on the NS and the EW profile (Fig. 1), which provide a far greater source-receiver offset range and crossing ray area that are needed for extracting high-quality detailed velocity information, have been analyzed prior to this study.

The seismic source consisted of two linear arrays of 7 air guns towed at an average depth of 14 m with a total nominal volume of 6790 in^3. Three different types of short-period OBS were used to record the wide-angle data: 16 Canadian OBSs from Dalhousie University, 7 French OBSs from the Institut National des Sciences de l'Univers du CNRS, and 9 micro OBSs from the National Central University of Taiwan. All the OBSs recorded continuously at a sampling rate of 250 Hz (4 ms) with one hydrophone and a 3 orthogonal component geophone. The OBS spacing ranges from 3 to 10 km. For presentation purposes, OBS names used during the survey were converted to sequential numbers (Fig. 1; Table S1). OBSs north of OBS 1, and between OBSs 3 and 4, OBSs 13 and 14, and OBSs 31 and 32 were lost during the survey or recorded unusable

data. The white circles in Figure 1 are the 32 OBS instruments used for the modeling. These OBSs form the two ~150 km long wide-angle seismic profiles. The EW profile (SMOO35) lies in the spreading axis direction, and the NS profile (SMOO33) is orthogonal to and crosses the spreading axis (Fig. 1a). The NS profile cuts through the inferred detachment faults and practically all of its OBSs lie within the previously mapped smooth seafloor. The EW profile is presumed to transition from volcanic seafloor in the west to exhumed mantle at the seafloor in the east.

3.2 Data processing

The OBSs were relocated to their true positions on the seafloor (more information in Supporting Information) and the data were bandpass filtered using a minimum phase trapezoidal band-pass filter with corner frequencies 1-5-18-25 Hz. PASTEUP software (Fujie et al., 2008) was used to manually pick the first break of arrivals on the OBS records. Two examples of OBS gathers for the NS and the EW profiles, with and without picks, are shown in Figure 2. More examples are shown in Supporting Information (Figs. S1-S4). The picking was carried out on unfiltered data as much as possible, with the filtered data used only to extend the picks to further offsets. Where first arrivals are not clear at long offsets, arrivals of the first water multiple were picked where possible and then time-shifted until picks from the multiple for near and/or mid offsets coincided with equivalent picks for the first arrivals. The 2D bathymetry from a previous multibeam survey (Cannat et al., 2006) was plotted in a separate window above the OBS data window as a function of model distance and source-receiver offset to help guide the picking process and identify seafloor diffractions. First arrivals were picked to offsets of up to ~90 km along the NS profile, and ~60 km along the EW profile. Assigned pick uncertainty is offset dependent as follows: 30 ms for high-quality waveforms at offsets <6.5 km; 60 ms for offsets between 6.5 km and 12 km; 100 ms for offsets between 12 km and 20 km; 120 ms for offsets >20 km; and 150 ms for time-shifted multiple arrival picks. A total of 6,523 and 4,193 first arrival picks were made for the NS and the EW profile, respectively. Secondary arrivals, such as Moho reflections, were not found in the OBS records, and sediment arrivals were negligible.

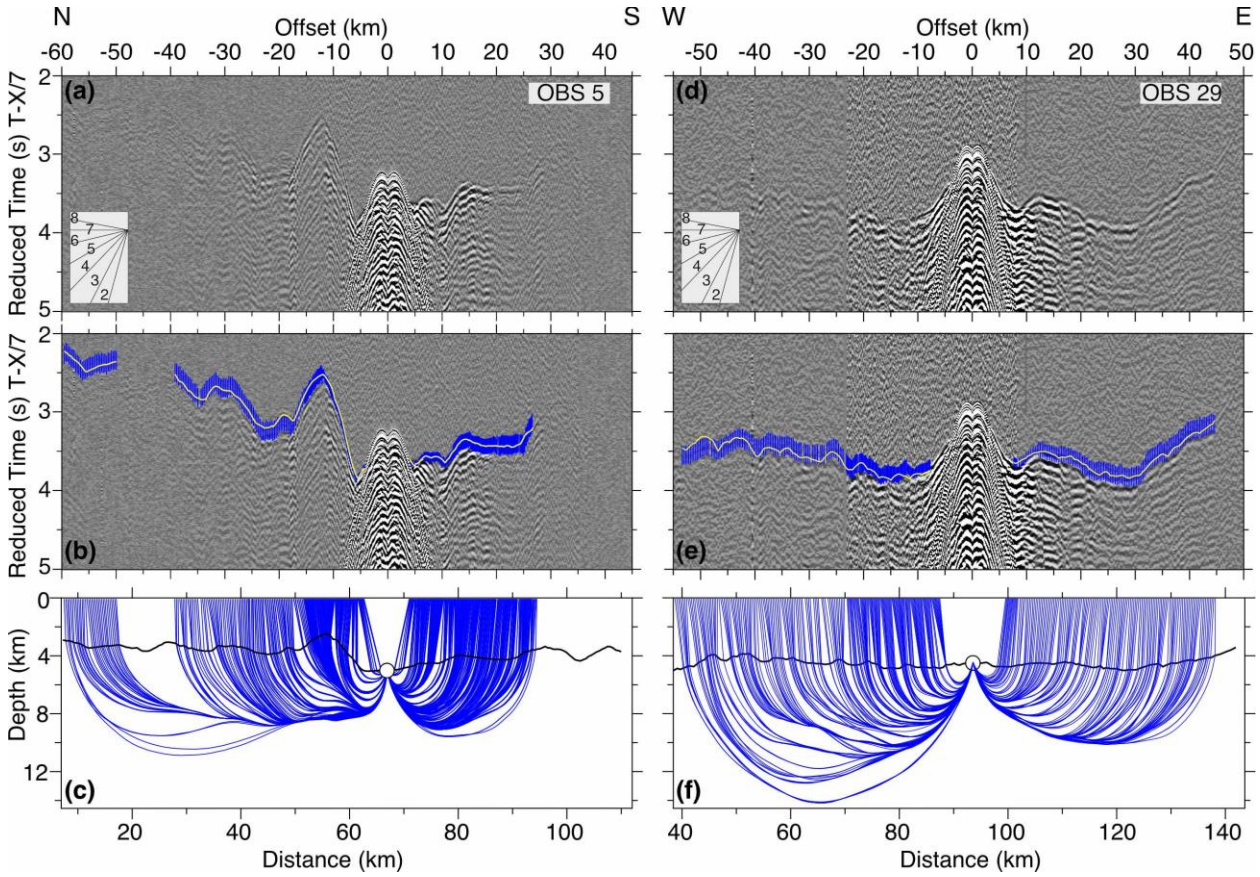

Figure 2. Example OBS gathers for the NS and EW profiles (a and d) are shown together with related first arrival traveltime picks (b and e) and calculated ray paths (c and f). (a) Hydrophone data for OBS 5 on the NS profile and (d) vertical geophone data for OBS 29 on EW profile after application of a reduction velocity of 7 km/s and band-pass filtering (1-5-18-25 Hz). Insets show the linear moveout of different phase velocities in km/s. (b and e) Same as a and b but with picked (centers of blue error bars) and modeled (yellow curves) first arrival traveltimes superimposed. Synthetic traveltimes and raypaths were computed by ray tracing through the final velocity model. (c and f) Raypath diagram for the modeled first arrival traveltimes in b and e. Black thick line is the seafloor and white circles with thin black outlines show the OBS locations.

3.3 Traveltime tomography

We performed P-wave traveltime tomography using TOMO2D (Korenaga at al., 2000). Traveltimes of P-wave first refracted arrivals and later Moho reflection arrivals (*PmP*) are commonly used for joint inversion of the regional 2D velocity structure in a sheared mesh model hung from the seafloor (e.g. Watremez et al., 2015). We, however, do not model the Moho reflector because of the lack of *PmP* arrivals in the data. In the TOMO2D method, forward modeling is first applied to find the shortest raypath from the shot to the receiver for each arrival, followed by a least-squares regularized inversion, in which the starting velocity model is perturbed and updated until the targeted chi-squared (χ^2) or the set number of maximum iterations is reached (Korenaga et al., 2000). Application of smoothing and optional damping constraints is used to regularize the iterative inversion process (Korenaga et al., 2000). Thus,

damping and smoothing weighting factors control the data fitting and the smoothness of the model, and similarly, the correlation lengths for the velocity nodes control the inversion stability. The final TOMO2D product is a minimum-structure smooth velocity model, meaning that minimum a priori information is used to resolve the minimum or simplest structure needed to explain the data. This approach reduces subjective input from the interpreter in the development of the final tomographic model.

Cells in our models, which are 160 km long and 30 km deep, are 1 km wide and 500 m high. The starting 1D velocity model is based on the 1D average velocity of Momoh et al. (2017) and the average velocity structure reported at other ultraslow-spreading centers bearing serpentinized mantle domains (e.g. Grevemeyer et al., 2018b; Van Avendonk et al., 2017). We opted for simplicity and, after taking into consideration the expected geology, settled on a 1D starting velocity model with 3 velocity-depth points: 4 km/s velocity at the seafloor, 6.5 km/s at 2 km depth below the seafloor (dbsf), and 8.0 km/s at 5 km dbsf. For consistency, the same 1D starting velocity model extended in 2D by hanging it off the seafloor was used for both orthogonal profiles. Figures 3a and 3d show the starting velocity model extended in 2D for both the NS and EW profile, respectively. For the NS profile, the starting velocity model produced a χ^2 of 11.97 and an RMS traveltime residual of 208 ms. For the EW profile, it produced a χ^2 of 15.37 and an RMS traveltime residual of 261 ms. We set our inversion to run 5 iterations and use the same parametrization values for both profiles to prevent modeling inconsistencies (more information in Supporting Information).

4 Results

4.1 Velocity models

Figure 3b shows the final velocity model for the NS profile. The model is shown over the areas with ray coverage and the calculated raypaths are shown in Figure 3c overlaying the final velocity model. The model converges to an RMS traveltime residual of 53 ms and a χ^2 of 1.10. Similarly, the final velocity model of the EW profile is shown in Figure 3e and the calculated raypaths are shown in Figure 3f. The EW model converges to an RMS traveltime residual of 55 ms and a χ^2 of 0.86. Figure S5 shows the evolution of χ^2 as a function of iteration number for both models. Most of the lateral and vertical velocity variations are found in the central parts of the models, below the areas covered by the OBSs, and therefore in the areas where there are crossing raypaths (Figs. 3c and 3f). Toward the profile ends, which are sections covered by shots but no OBSs, or sections with no crossing raypaths, the velocity structure in the final models mostly follows the seafloor topography and the starting velocity models.

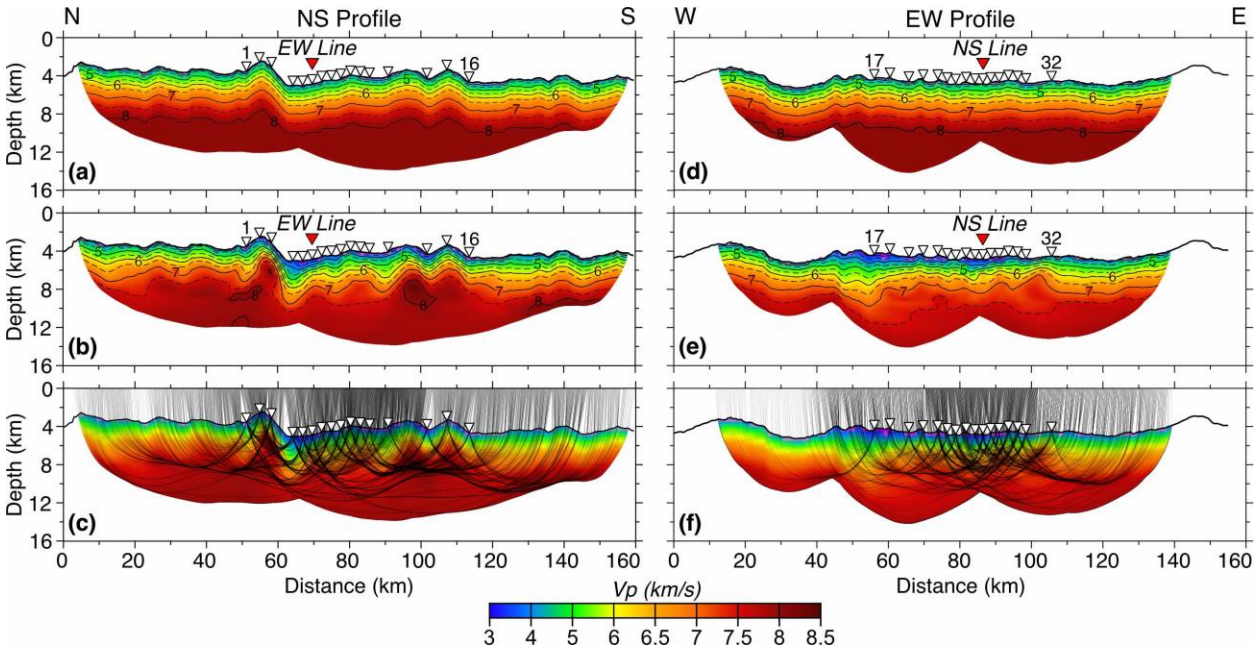

Figure 3. Results from first arrival traveltime tomographic inversion of the NS and EW profiles: (a, d) Starting velocity models; (b, e) final tomographic models; (c, f) raypaths (black lines) of the first arrivals traced through the final velocity models (b, e), for the NS and EW profiles, respectively. Iso-velocity contours are shown every 0.5 km/s in (a, b, d and e); solid black at every km/s and dashed in between. White inverted triangles show the positions of the OBSs on the seafloor. Red triangles show the location at which the profiles cross each other.

Traveltimes are well fitted at all model distances (Figs. S6a and S6b) with the majority of traveltime residuals, calculated as the difference between the observed and calculated traveltimes, reduced by the inversion to ±60 ms (Figs. S6c and S6d).

The final velocity models (Figs. 3b and 3e) show that seismic velocities increase rapidly with depth with velocities ranging from ~3.5 km/s at the seafloor to 7 km/s at 1.5–5.5 km dbsf at the NS profile, and from ~3 km/s at the seafloor to 7 km/s at 2-6 km dbsf at the EW profile. The NS profile reaches velocities in the range of 7.8-8.4 km/s, while the EW profile only reaches velocities in the range of 7.6–7.8 km/s. The NS profile shows greater lateral changes in the velocities than the EW profile, including a sharp lateral change (horizontal gradient of ~1 s^{-1} at ~62 km model distance) at the highest topographic feature. Within the area of OBS coverage, the EW profile also shows a smooth trend of increasing velocities toward the East, which is accentuated between OBSs 30 and 32. Similarly, a distinct increase in the velocities is observed between OBSs 17 and 18. Both profiles show high vertical velocity gradient (velocity contours closely spaced) in upper sections of the models (velocities <7 km/s) and a considerably lower vertical gradient (sparse velocity contours) in deeper sections (velocities >7 km/s).

4.2 Uncertainty assessment

4.2.1 Checkerboard Tests

We assess the resolution of our models with checkerboard tests as follows. Checkerboard patterns for a set of different horizontal and vertical cycle lengths with a ±5% periodic velocity perturbation are added to our two final velocity models. The chosen cell widths and heights are:

25x10 km (Figs. 4a and 4d), 12.5x5 km (Figs. 4b and 4e), and 5x2.5 km (Figs. 4c and 4f). The perturbed velocity models are used as the starting velocity models for the inversions. The recovered perturbations are obtained by subtracting the input velocity models from the corresponding final inverted velocity models for different cell sizes. The extent of perturbation recovery at any particular section of our models is a measure of resolvability of corresponding velocity anomalies for that model area. The input and inverted perturbation models are compared for the two profiles in Figure 4. Full-size checkerboard test figure is included in the SI (Fig. S7). Large structures are resolved across the profiles where there is any ray coverage (Figs. 4a and 4d). Structures 12.5 km wide and 5 km high are resolved in the areas below the seafloor encompassing the first and last OBS location to depths of ~5 km. In these central areas, structures as small as 5x2.5 km are also resolved but the depth or resolvability below the seafloor is reduced to ~2–3 km. In all the checkerboard tests, the resolved cells are smeared toward profile ends and with increasing depth, with the resolution progressively declining.

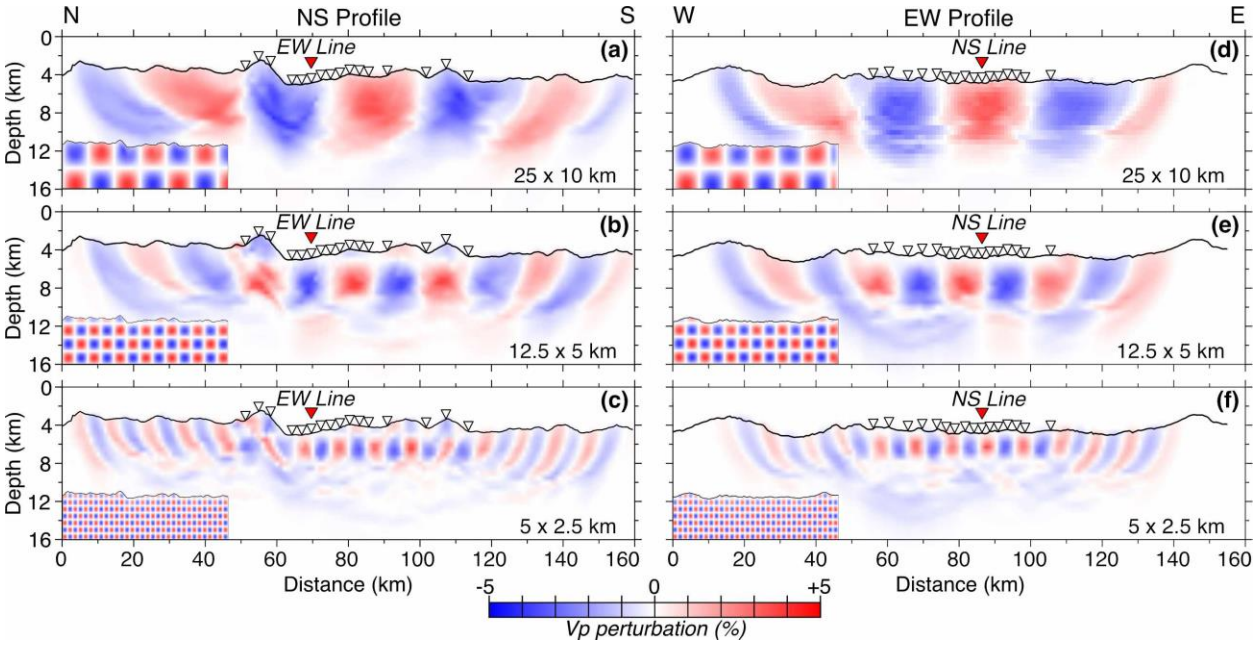

Figure 4. Checkerboard resolution tests for the NS (left column) and EW (right column) profiles for perturbation cells: 25 km wide x 10 km high (a and d), 12.5 km wide x 5 km high (b and e), 5 km wide x 2.5 km high (c and f). The input perturbed model is shown in the bottom left inset and the recovered perturbed model is the full-size figure. White and red inverted triangles as in Figure 3 caption.

4.2.2 Monte Carlo Analysis

We run a nonlinear Monte Carlo analysis (e.g. Tarantola, 1987) to estimate velocity uncertainty across our models following the strategy of Korenaga et al. (2000). For this analysis, the input velocity model (or starting velocity model) is randomized to create a set of 100 different input models (Fig. S8). This is done by randomizing the velocities of the three nodes of the starting velocity model within a ±6% range and by randomizing the depths to the two sub-seafloor layer interfaces or inflection points within a ±1.1 km range. The 100 randomized 1D starting velocity models are used to form 100 randomized 2D starting velocity models and run

100 inversions (for both NS and EW profiles) using the same inversion parameters applied to calculate the final velocity models (Figs. 3b and 3e). The resulting tomographic models are averaged to produce average velocity models for the NS and EW profiles (Figs. 5a and 5d) and compute standard deviations of the P-wave velocities across these models (Figs. 5b and 5e). The results show that the inversion process is stable as the average velocity models (Figs. 5a and 5d) are very similar to the final velocity models (Figs. 3a and 3d) for both profiles. The standard deviation of seismic velocities for most of the lithosphere at central parts of the models is <~0.1 km/s (Figs. 5b and 5e). Larger standard deviations are observed in the areas that are less well resolved as indicated by the checkerboard patterns (Fig. 4), in areas with lower ray density (Figs. 5c and 5f) and especially where there are no crossing rays (Figs. 3c and 3f), and below the seafloor where no instruments were deployed. The ray density is presented by the derivative weight sum (DWS; Toomey & Foulger, 1989), a nondimensional relative indicator of ray coverage.

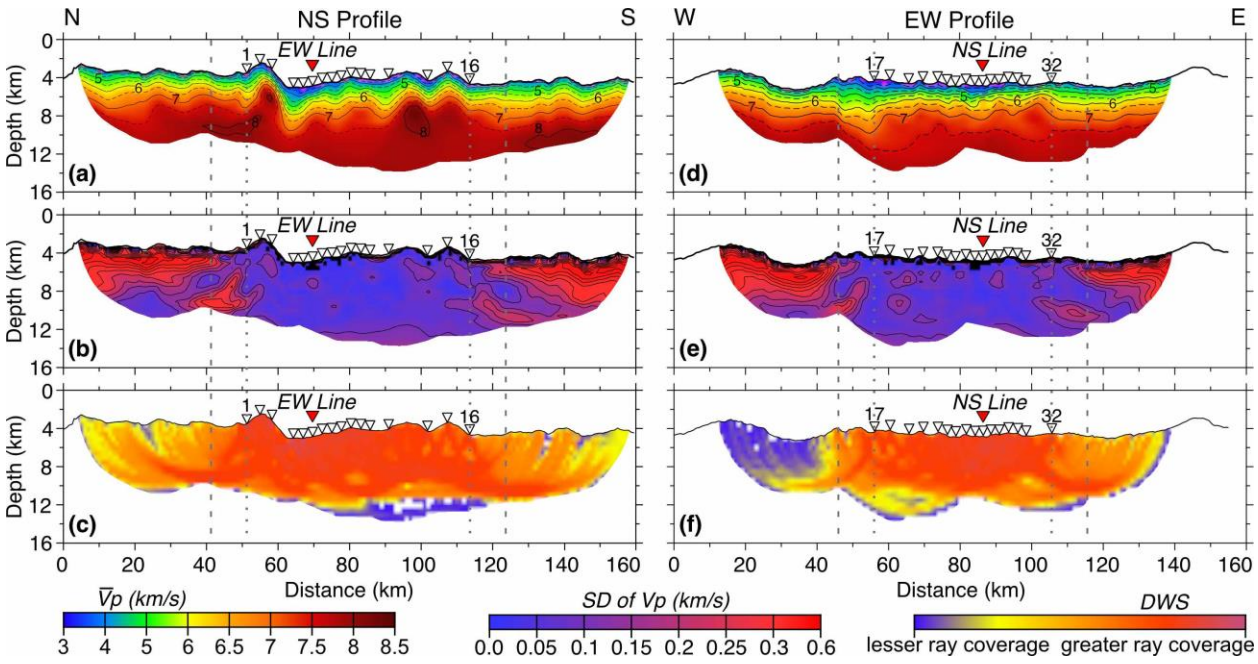

Figure 5. Results from the Monte Carlo analysis. Averaged final velocity models for the NS (a) and EW (d) profiles. Iso-velocity contours are shown every 0.5 km/s in (a and d); solid black at every km/s and dashed in between. Standard deviation of the P-wave velocity calculated via the Monte Carlo analysis for the NS (b) and EW (e) profiles. Solid black contours are shown every 0.05 km/s in (b and e). Derivative weight sums (DWS) indicating the ray coverage for the NS (c) and EW (f) profiles. In all panels, the dotted light grey vertical lines mark the end of the best resolved areas, and the dashed light grey vertical lines mark the ends of the well resolved areas. White and red inverted triangles as in Figure 3 caption.

4.3 Derivatives of the velocity models

To aid the discussion, we plot 1D velocity-depth functions (Fig. S9) extracted at every 1 km distance within the best resolved areas of the two average velocity models (Figs. 5a and 5d). We use these functions to determine the average 1D velocity-depth functions and the extent of the velocity-depth envelopes for both profiles (Fig. S9). We further augment our interpretation

by computing and plotting velocity anomalies (Figs. 6a and 6c) and vertical velocity gradients (Figs. 6b and 6d) for both the NS and EW profile. The 2D velocity anomalies are calculated as the difference between the average velocity models (Fig. 5a and 5b) and the respective average 1D velocity-depth functions (Fig. S9). The vertical velocity gradients are calculated by computing the central first derivative of the average velocity models (Fig. 5a and 5b).

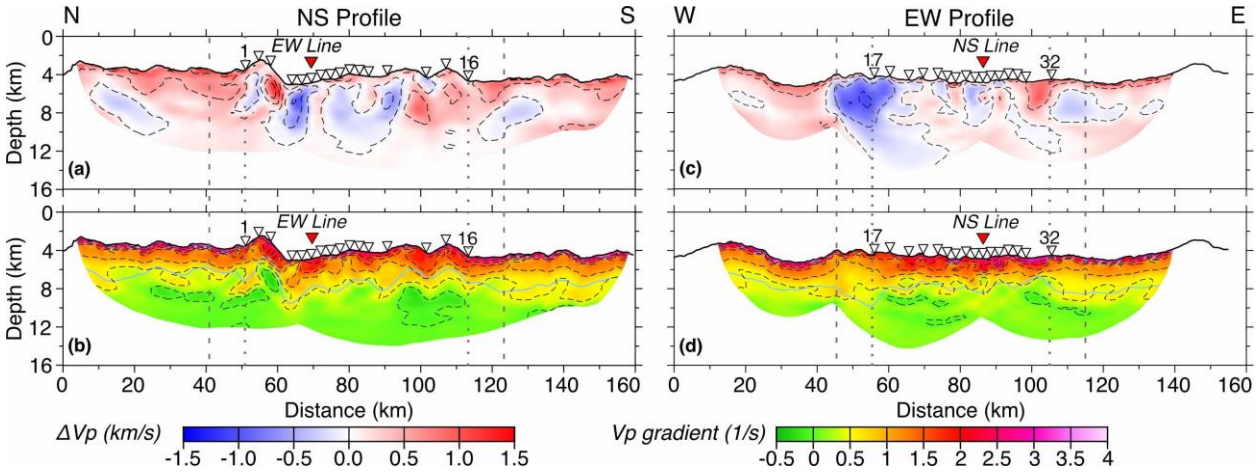

Figure 6. Velocity anomaly (top panels) and velocity gradient (bottom panels) results for the NS and EW profiles, respectively. Dashed black contours are shown every 0.5 km/s in (a and c) and every 0.5 s^{-1} in (b and d). The depth to the 7 km/s velocity contour is shown in (b) and (d) in a solid light blue line. White and red inverted triangles as in Figure 3 caption. Vertical dotted and dashed light grey lines as in Figure 5 caption.

5 Discussion

The final and average P-wave tomographic velocity models for the NS and EW profiles give insight into the subsurface structure of the SWIR at 64°30'E. In the following subsections, we discuss (1) the ridge structure and the distribution of the active fault and the older and now inert detachment faults; (2) the inferred lithospheric composition and its anisotropy; and (3) the velocity structure in our study area in the context of the known velocity structure elsewhere at the SWIR. We limit our discussion only to the geological structures that can be resolved as indicated by the checkerboard tests, and the areas of the velocity models that show standard deviations of <~0.1 km/s (Figs. 5b and 5e) and/or high ray coverage (Figs. 5c and 5f). This effectively limits our detailed interpretation to the best resolved areas (within the dotted light grey vertical lines in Fig. 5) with crossing rays and OBSs on the seafloor (51 to 114 km model distance for the NS profile and 55 to 106 km for the EW profile), with the regional interpretation extended to include the well resolved areas (within the dashed light grey vertical lines in Fig. 5) found up to ~10 km away from the first/last OBS on both profiles, as indicated by the Monte Carlo analysis results (Fig. 5).

5.1 Ridge structure

5.1.1 Delineation of detachment faults on the NS profile

The information extracted from the NS profile (Figs. 5a, 6a and 6b), which cuts across the SWIR at 64°30'E, is particularly useful for subsurface identification of the active and

abandoned detachment faults. We first interpret a sharp lateral change in the velocities (a horizontal gradient of ~1 s^{-1} at ~62 km model distance; Figs. 5a and 6a) and a high vertical velocity gradient (1.5–2.5 s^{-1}; Fig. 6b) coincident with the shallow section (top 2 km, i.e depth 0-2 km below seafloor) of the highest topographic feature (~51-62 km model distance) as the seismic expression of an active axial detachment fault (hereafter *D1*; Fig. 7). This bathymetric high is characterized by higher velocity than the surrounding regions (Fig. 5a) and its top surface has previously been interpreted as an active axial detachment fault based on side-scan sonar (Sauter et al., 2013), bathymetric and kinematic analysis (Cannat et al., 2019; Reston, 2018), and seismic reflection data (Momoh et al., 2017, 2020). Therefore, our velocity model supports these earlier interpretations as it shows the footwall exhuming (or bringing up to shallow depth) rocks of high velocities, those corresponding to lithologies typically found at greater depths, which become superimposed by the lower velocity rocks of the hanging wall at the topographic low immediately south. This north-south transition at ~62 km model distance from the detachment footwall to the detachment hanging wall is characterized by an abrupt decrease in the vertical gradient, from a high of 1.5–2.5 s^{-1} to a low of 0.5–1.0 s^{-1}, as well as by a switch in polarity of the largest velocity anomaly, from 1.5 km/s to -1.5 km/s.

Elsewhere, the NS profile exhibits smoothly varying low to moderate vertical velocity gradient values (<1.5 s^{-1}), except for several locations that show similar lateral changes in the vertical velocity gradient to D1, with higher vertical gradients (1.5–2.0 s^{-1}) juxtaposed with lower gradients (0–1.0 s^{-1}) at alike depths (~top 2 km). These are found at model distances of about 50 km, 74 km, 87 km, 101 km, and 113 km (Fig. 6b). The velocity anomalies (Fig. 6a) at these model distances also show a similar change to D1, with a switch in the polarity from positive to negative anomaly, except at 50 km where the switch in polarity is reversed. Aditionally, the velocities (Fig. 5a) across the profile show a repeat drop pattern that coincides with the changes observed in the vertical velocity gradient and velocity anomalies. While the identified vertical velocity gradient, velocity, and velocity anomaly changes are not as pronounced as for the interpreted active detachment fault D1, they are clearly recognizable and we interpret them to indicate the subsurface location of the abandoned detachment faults (*D2* at ~50 km, *D3*' at ~74 km, *D3* at ~87 km, *D5* at ~101 km, and *D7* at ~113 km; Fig. 7b).

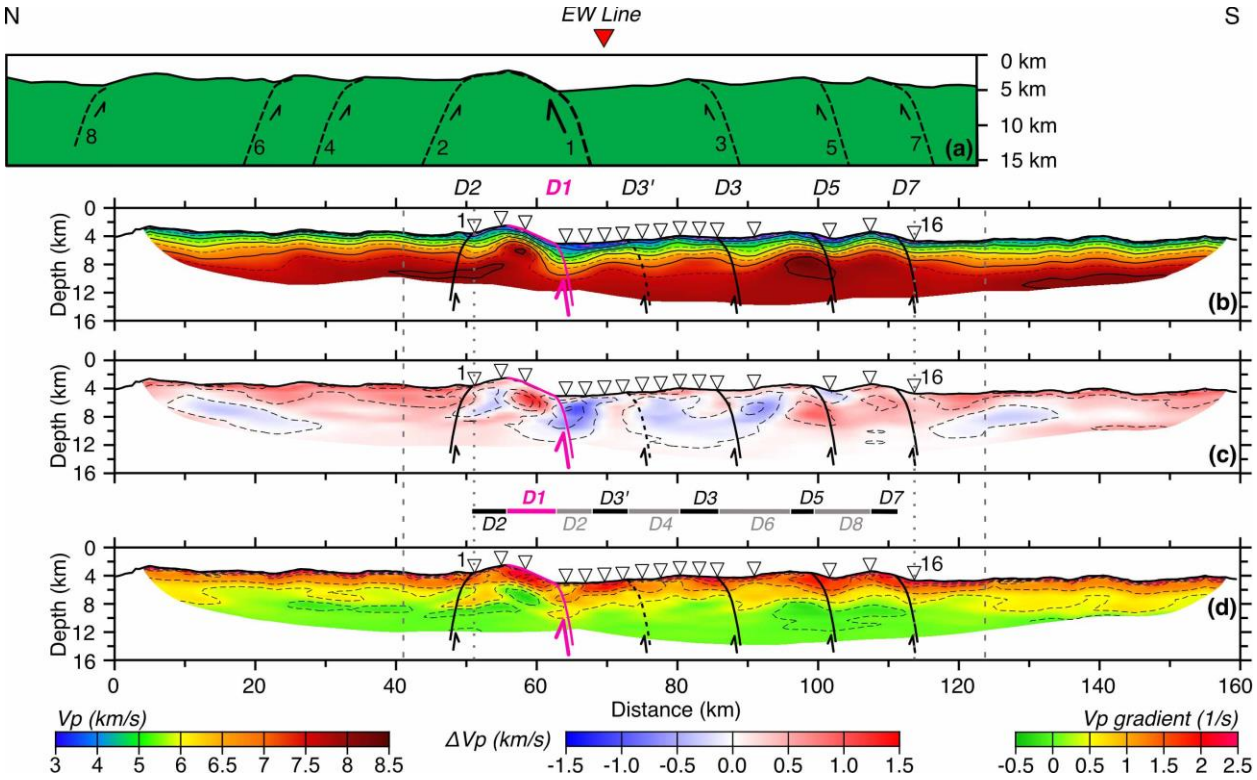

Figure 7. Comparison of a (a) conceptual model based on previous interpretations (Cannat et al., 2019; Reston, 2018; Sauter et al., 2013) depicting the sequence of flipping rolling-hinge faults (black dashed lines) along the NS profile and (b) the average velocity model from Figure 5a, (c) velocity anomalies from Figure 6a, and (d) vertical gradient from Figure 6b, with interpreted locations of corresponding faults (solid lines) for the best resolved area (51-114 km). In (a), previously interpreted faults are numbered 1–8 from youngest to oldest. In (b, c, and d) the identified faults are named *D2*, *D1*, *D3*', *D3*, *D5*, *D7*, and are equivalent to faults *2*, 1, 3, 5, and 7 in (a) omitting *D3*' that is not inferred in (a). *D* stands for detachment. *D1* is the active detachment fault (solid pink line) and the fault numbers increase sequentially to describe older abandoned faults (solid black lines). Inset between (c) and (d) shows the interpreted extension of each detachment footwall surface located on the seafloor. The thin rectangle in pink limits the extension of *D1* footwall surface, the black rectangles limit the extension of *D2*, *D3*', *D3*, *D5* and *D7* footwall surfaces, and the grey rectangles limit the extension of *D2*, *D4*, *D6*, and *D8* hanging wall surfaces. Iso-velocity contours are shown every 0.5 km/s in (b); solid black at every km/s and dashed in between. Dashed black contours are shown every 0.5 km/s in (c) and every 0.5 s^{-1} in (d). White and red inverted triangles as in Figure 3 caption. Vertical dotted and dashed light grey lines as in Figure 5 caption.

5.1.2 Comparison with earlier interpretations

In Figure 7, we compare our interpretation on the location of the detachment faults with that of previous interpretations (Cannat et al., 2019; Reston, 2018; Sauter et al., 2013), which are primarily based on observed bathymetric features, i.e. the location of the breakaway and emergence points on the fault surfaces. For simplicity, we list the detachment faults previously inferred from 1 to 8, with 1 being the youngest and 8 being the oldest fault (Fig 7a). Our velocity

model (Fig. 7b), the velocity anomalies (Fig. 7c), and the vertical velocity gradient (Fig. 7d), provide supporting evidence for the existence of faults 1–3, 5 and 7. The reverse polarity in the pattern observed in the velocity anomalies at ~50 km model distance (Fig 7c), at the interpreted location of *D2*, coincides with the previously interpreted location of fault 2 (Cannat et al., 2019; Reston, 2018; Sauter et al., 2013), only offset by ~1 km south. Fault *D2* was active prior to *D1* and thus it shows opposite polarity. Similarly, the interpreted location for fault *D1* is comparable to the location of the previously interpretated fault 1, only offset by ~1 km north (Fig. 7). Previously interpreted locations of faults 5 and 7 are identical to the interpreted locations of *D5* and *D7* in this work, respectively, while fault 3 is offset by ~4 km north from *D3* (Fig. 11). The locations of faults *D1* and *D3* are also consistent with previously identified south dipping reflectors in MCS data (Momoh et al., 2017, 2020) interpreted to be related to fault damage in the footwall. The results presented here also demarcate an abandoned detachment *D3'* that has not been inferred previously. Detachment *D3'* may have been missed in other models (Cannat et al., 2019; Reston, 2018; Sauter et al., 2013) because its seafloor expression shows a smoother emergence topography in comparison to the other interpreted faults based on bathymetry. One possible cause for this is a relatively short lifespan of the *D3'* fault, which precluded full development of the characteristic seafloor geometry of a detachment fault. Alternatively, the velocity signature observed at ~74 km model distance may possibly be related to recent extensional damage occurring in the hanging wall of *D1* as proposed by Momoh et al. (2020), since no south dipping reflectors related to this fault are imaged in MCS data (Momoh et al., 2017). However, given the resolution of our model, the presence of fault *D3'* provides an explanation that is more consistent with the velocity, velocity anomaly, and vertical gradient patterns observed at the locations of other interpreted faults (Figs. 7b, 7c, and 7d).

For our study area, Cannat et al. (2019) estimated the duration of the active deformation period for each detachment fault. The active life for these detachments ranges from 0.6 Myr to 2.8 Myr, with an average life of 1.35 Myr. Our interpretation of an additional detachment fault (*D3'*; Fig. 7) combined with the adjustment in the location of *D3* calls for a reevaluation of these age numbers. However, we can only estimate total fault longevity for detachments *D1* and *D2*, and partial longevity for faults south of *D1* since our NS velocity model does not resolve the location of the faults north of *D2* (Table 1). Like Cannat et al. (2019), we estimate the partial and total fault lifespans based on the horizontal distance between faults' emergence and breakaway points (Table 1). The inset shown in between Figures 7c and 7d illustrates the interpreted extension of each detachment footwall surface on the seafloor used for our calculations. Portions of each abandoned fault footwall are located both north and south of the spreading axis, except for the active detachment (*D1*) that has not yet been cut off by a new master fault and carried away from the axis. Portions of *D4*, *D6* and *D8*, the faults inferred further north of *D2* but not resolved by our velocity model, are also considered based on earlier interpretations of seafloor data (Cannat et al., 2019; Reston 2018; Sauter et al., 2013) to estimate the ages in Table 1. Our calculations point to a duration of ~0.7 Myr for *D2*, half the previously suggested age, and ~0.5 Myr for *D1*, larger than the previously suggested age (0.3 Myr).

Detachment # ***(Youngest to oldest)***	**Dip**	**Horizontal distance from fault emergence to**	**Horizontal distance from fault breakaway**	**Estimated partial fault duration**	**Estimated total fault duration** ***(Myr)***

		adjacent fault breakaway *(km)*	**to adjacent fault emergence *(km)***	**based on distance *(Myr)***	
D1 *(active)*	South	7.1	0	0.51	0.51
D2 *(North of D1)*	North	5.0	-	0.36	0.72
D2 *(South of D1)*	North	-	5.1	0.36	
D3'	South	5.1	*Unknown*	0.36	*Unknown*
D4	North	*Unknown*	7.3	0.52	*Unknown*
D3	South	5.5	*Unknown*	0.39	*Unknown*
D6	North	*Unknown*	10.2	0.73	*Unknown*
D5	South	3.4	*Unknown*	0.24	*Unknown*
D8	North	*Unknown*	8.0	0.57	*Unknown*
D7	South	3.9	*Unknown*	0.28	*Unknown*

Table 1. Estimated detachment fault longevity based on the horizontal distance between faults' emergence and breakaway locations of the inferred faults across the profile SMOO33 (NS profile).

5.2 Lithospheric composition

5.2.1 Exhumed mantle area

In order to relate the modeled velocities to the subsurface lithology, we assume that the investigated area is composed of exhumed mantle rocks ranging from variably serpentinized and fractured peridotites at shallower depths, to unaltered peridotites at greater depths. This is followed by conversion of the seismic velocities along the NS and EW profiles (Figs. 5a and 5d) to degree of serpentinization (Figs. 8a and 8b) using a linear relationship for partially-serpentinized peridotites (Fig. 8c) from Carlson & Miller (2003). These authors used empirical data (Christensen, 1978, 1996; Miller & Christensen, 1997) to evaluate how the relationship between P-wave velocities and the degree of serpentinization changes with different confining pressure and temperature. We choose the relationship for a temperature of 300°C, in agreement with the high serpentinization temperatures suggested for the rock samples analyzed along the NS profile (Rouméjon et al., 2014). Albeit converting seismic velocities to degree of serpentinization is a simplification of the causes for the velocity heterogeneities, especially at the top of the model, it allows us to discuss how deep serpentinization may extend and what may control such depth.

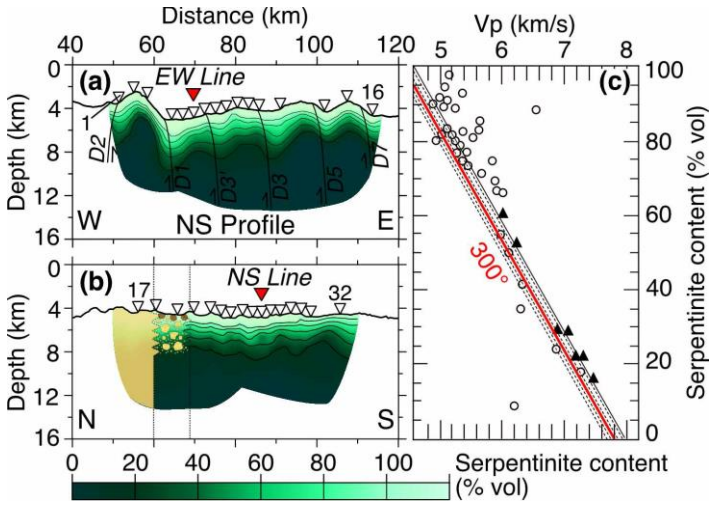

Figure 8. Estimated degree of serpentinization for the NS (a) and EW (b) profiles based on their tomographic velocities (Figs. 5a and 5d) and the linear relationship (c) of serpentinite content with P-wave velocity from Carlson and Miller (2003) for a temperature of 300°C, in agreement with oxygen isotopes studies in the area (Rouméjon et al., 2015). Black triangles in (c) are laboratory measurements of P-wave velocities in serpentinized peridotites at 25°C and at 200 MPa and open circles are velocity measurement at other confining pressure (up to a 1000 MPa). Carlson & Miller (2003) collected data points from several studies (Christensen, 1978, 1996; Miller & Christensen, 1997). Dashed lines show the approximate relationships at temperatures of 100, 200, 300, 400, and 500°C corrected from the best fitting relationship measured at 200 MPa (solid black line). In (a) the solid black lines show the detachment faults' locations interpreted in Fig. 7. In (b) the dotted lines show the location at which there is a change in the lithosphere (volcanic before 59 km, non-volcanic after 69 km, and transitional in between) as discussed in the text. Solid black contours in (a and b) show serpentinite content at every 20% vol. White and red inverted triangles in (a) and (b) as in Figure 3 caption.

While our assumption of the exhumed mantle domains throughout the study area is a simplification of the true geology, it is supported by several lines of evidence and justified by our intent of carrying out a first-order interpretation of the subsurface geology. First, earlier rock sampling of the seafloor in our study area (Rouméjon et al., 2014; Sauter et al., 2013) has predominately retrieved peridotites and the extent of the mapped smooth seafloor (Cannat et al., 2006) (Fig. 1), interpreted to represent exhumed mantle domains, covers majority (~¾) of the area along the NS and EW profiles contained by the OBS instruments. Second, no reflection Moho has been identified in the pseudo-3D MCS dataset by Momoh et al. (2017), which indicates the lack of a distinct and seismically-well characterized Moho in our study area. Reflection Moho is often well imaged in upper oceanic lithosphere formed at faster spreading mid-ocean ridges where a 3-layer mafic oceanic crust tops the ultramafic uppermost mantle (e.g. Aghaei et al., 2014; Bouhalanis et al., 2020). Third, no wide-angle Moho reflected arrivals (*PmP*) are identified in the OBS data examined in this work, and these arrivals are routinely observed and picked in data collected worldwide in oceanic lithosphere formed at faster spreading rates (e.g. Canales et al., 2000; Horning et al., 2016). Furthermore, the lack of *PmP* arrivals in our study area is consistent with observations from other ultraslow spreading ridges dominated by magma starved spreading conditions (Grevemeyer et al., 2018b).

We interpret the uppermost lithosphere to be composed of highly fractured and fully serpentinized peridotites at the top with a gradual decrease in pore space volume and serpentinization degree to unaltered peridotites at depth (Figs. 8a and 8b). The velocities lower than 4.5 km/s at the top of the model may be representative of peridotites that are fully serpentinized and heavily fractured. Geologically, these low velocities could also be representative of basalts. However, this possibility is highly unlikely because, whereas scattered low-volumetric basalts may be found across the study area (Sauter et al., 2013), the results of the extensive seafloor studies and the lack of Moho reflections in both wide-angle OBS and MCS data (e.g. Cannat et al., 2006; Sauter et al., 2013; Momoh et al., 2015) clearly indicate that a continuous basaltic top layer is not present.

While our first order interpretation is comparable to that of Momoh et al. (2017), the higher resolution and lateral variability of the new results presented in this work make it possible to carry out a detailed interpretation. Serpentinization seems more extensive and penetrates deeper along the NS profile than the EW profile. For example, 20% serpentinization extends to up to ~5 km dbsf on the NS profile and up to ~3–4 km dbsf on the EW profile, with the anomaly being the location of the active detachment fault (*D1*) footwall where the 20% serpentinization contour is found at the shallowest depths of ~1.5–2 km dbsf (Figs. 8a and 8b).

The change from relatively large and quickly decreasing vertical velocity gradients (1.5-2.5 s^{-1}) at velocities <7 km/s, to relatively low and gradually decreasing vertical velocity gradients (<0.5 s^{-1}) at velocities >7 km/s (Figs. 6b and 6d) likely illustrates a change in the porosity and permeability regime that impacts the serpentinization process for the upper and lower sections of the profiles. These low and gradually decreasing vertical velocity gradients within deeper sections of the models also indicate that the Moho transition is not an abrupt serpentinization or alteration front, as has been suggested for the study area and elsewhere along the SWIR (e.g. Dick et al., 2019; Mével, 2003; Minshull et al., 1998, 2006), but rather a gradual transition from hydrated peridotites to unaltered peridotites. The smoother gradient of seismic velocities above 7 km/s in the EW profile suggests a more uniform upper mantle in comparison to the NS profile.

From Figure 8a, we further decipher the following: (i) Despite the similar penetration depth of serpentinization on both sides of individual detachment faults, for similar depths on both sides of the detachment, serpentinization is more pervasive in the hanging walls than in the footwalls. This is possibly due to the continuous exhumation of the footwalls that leaves hanging walls longer exposed to water at temperatures that are more optimal for the serpentinization to take place (e.g. *D1*, Fig. 8a); (ii) The depth and degree of serpentinization depends on the length of time the detachments were active. For example, amongst the abandoned detachments south of *D1*, the 20% serpentinization contour reaches deeper levels around faults *D3'* and *D3* than around *D5* and *D7*, which agrees with the estimated longer active life for faults *D3'* and *D3* (Table 1). Therefore, we suggest that the bulk of the serpentinization occurs while detachment faults are active, with much diminished alteration after the lithosphere migrates off-axis. The longer a particular detachment is active, the deeper serpentinization reaches due to both more extensive deformation of the fault walls resulting in greater porosity and permeability and longer exposure to seawater. The overall increase in velocity and, therefore, decrease in estimated degree of serpentinization from the active to abandoned detachment faults is possibly caused by a reduction in porosity by closure of cracks and fractures once fault activity stops and the fault moves away from the ridge axis.

5.2.2 EW transition from exhumed mantle to volcanic seafloor

Earlier work on seafloor mapping in the study area (Cannat et al., 2006) indicated that the EW profile crosses a transition within the uppermost lithosphere from exhumed and serpentinized ultramafic mantle domains in the east to volcanic and magmatic mafic domains in the west (Fig. 1). This transition was initially interpreted to occur at the OBS 25 location (model distance ~84 km; Fig. 1) (Cannat et al., 2006). Cannat et al. (2019) later proposed a wider transitional domain from the detachment-dominated asymmetric topography, characteristic of non-volcanic seafloor, to the magmatic symmetric topography, characteristic of volcanic seafloor. The authors examined four ridge-perpendicular bathymetric profiles spread over a distance of ~50 km and observed a change in the seafloor topography across the profiles from ridge-asymmetric topography, indicative of non-volcanic seafloor, to ridge-symmetric topography, indicative of volcanic seafloor. The distance between the profile showing asymmetric topography and the closest profile showing ridge-symmetric topography is 32.6 km. A profile showing transitional bathymetry is found in between these two profiles, which led the authors to interpret that the transitional region occurs over a 20-30 km distance.

Our velocity, velocity anomaly, and vertical velocity gradient models (Fig. 9) also suggest a major change in the lithospheric structure and composition along the profile. This change occurrs over a distance of ~10 km between OBSs 18 and 20 (model distance ~59-69 km; Fig. 9). In Figure 9 we plot the limits of the interpreted volcanic and non-volcanic seafloor as proposed by Cannat et al. (2006, 2019) and in this study. The recent interpretation by Cannat et al. (2019) put the transitional area at model distance of ~54-86 km, which is wider but in broad agreement with the results from this work.

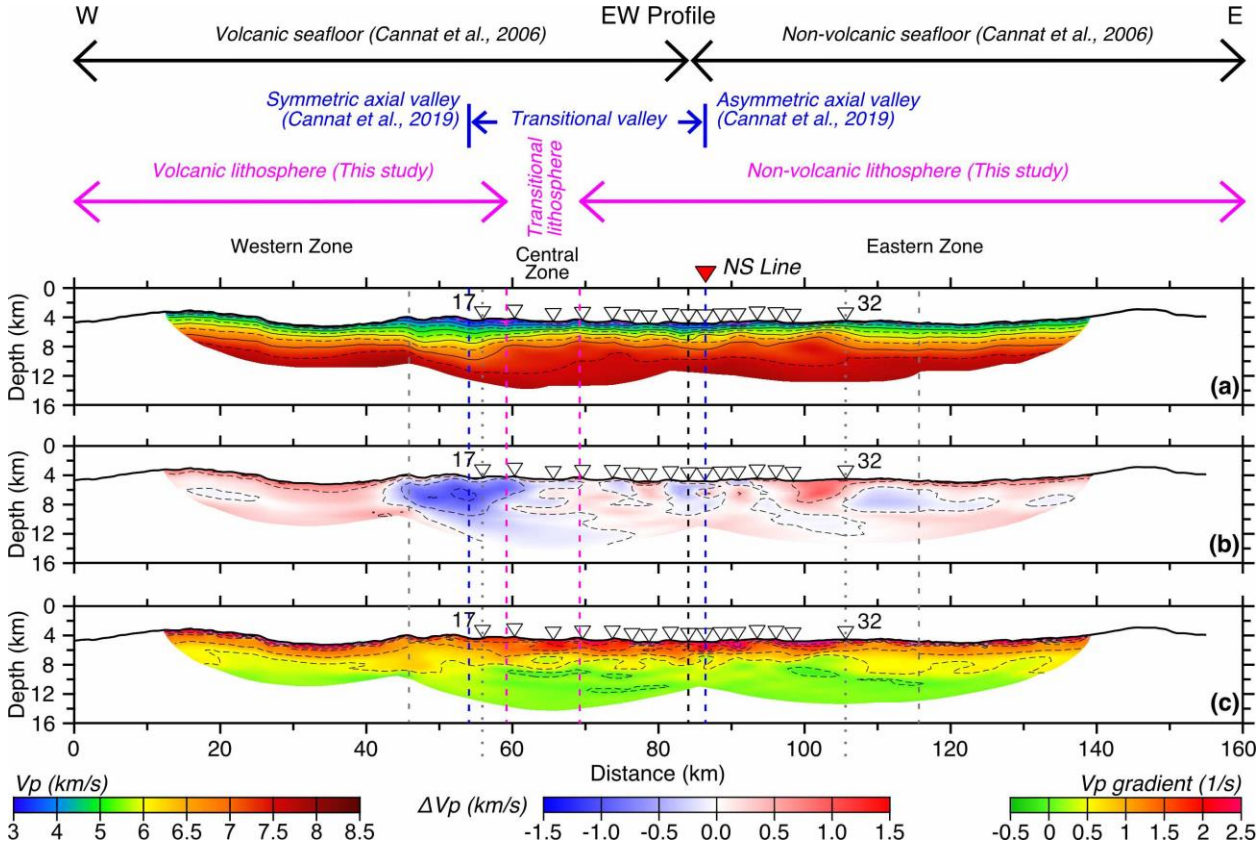

Figure 9. Comparison of the (a) average velocity model from Figure 5d, (b) velocity anomalies from Figure 6c, and (c) vertical gradient from Figure 6d, along the EW profile. Arrows in the top of the figure show the different interpretations of the proposed transition from volcanic to non-volcanic lithosphere: Cannat et al. (2006) in black, Cannat et al. (2019) in blue, and this study in pink. The blue short straight lines indicate the location of Cannat et al. (2019) bathymetric profiles that show contrasting symmetric and asymmetric axial valleys and constrain the transitional zone. The black, blue, and pink dashed lines extend the limits of the different interpretations across (a, b, and c). The pink arrows also delimit the three zones in the EW model: western, central, and eastern. White and red inverted triangles as in Figure 3 caption. Vertical dotted and dashed light grey lines as in Figure 5 caption.

The observed changes in velocity, velocity anomaly, and vertical velocity gradient divide the EW profile into three distinctive zones: eastern (model distance >69 km), central (model distance from 59 to 69 km), and western (model distance <59 km). The eastern zone shows high and laterally variable seismic velocities at shallow depths, reaching 4–4.5 km/s within 0.5 km dbsf and 7 km/s at depths 2–3.5 km dbsf (Fig. 9a), an overall positive velocity anomaly including a larger positive anomaly (0.5-1 km/s) at model distances 99–106 km (Fig. 9b), and a high vertical velocity gradient of 1–2 s^{-1} (Fig. 9c). These characteristics are consistent with exhumed and variably serpentinized mantle peridotites, where serpentinization extent diminishes as a function of depth. A low in the velocities that corresponds with a low velocity anomaly (Fig. 9b) and a more moderate vertical gradient than for the neighboring areas (Fig. 9c) is observed within model distances 81-86 km (below OBSs 24-26; Fig. 9a). We speculate that this is indicative of a ~5km-wide volcanic dike injection, a feature resolvable in our model (Fig. 4f), that could be responsible for the lower RMBA values (10–0 mGal) that led to the interpretation of this area and the area further west as volcanic seafloor (Cannat et al., 2006). Other smaller low velocity anomalies, e.g. below OBSs 21 and 22 (model distances 73–76 km; Fig. 9b) and below OBS 28 (model distances 90–92 km; Fig. 9b) may suggest the presence of additional smaller dikes that are not fully resolvable by our data. Detailed seafloor mapping in our study area with side-scan sonar shows small sparse lava patches on top of the exhumation surfaces (Sauter et al., 2013). Our results bolster the argument that the lava patches are erupted directly onto the exhumed surface by small offset high-angle normal faults (Cannat et al., 2019; Sauter et al., 2013), as opposed to being allochthonous rafted volcanic blocks transported to the surface off-axis by successive detachments (Reston, 2018). Furthermore, the presented evidence of volcanic dike injections within the "smooth-seafloor" favors the interpretation by Sauter et al. (2013) that the abandonment of the active axial detachment fault and consequent activation of the successive detachment fault may be a consequence of increased diking.

The western zone shows sharply lower seismic velocities that reach 3.5 km/s at 0.5 km dbsf and 7 km/s at 4–5.3 km dbsf (Fig. 9a), a large negative velocity anomaly of -1.5–-1 km/s (Fig. 9b), and a moderate to low vertical velocity gradient of 0.5–1 s^{-1} (Fig. 9c). These characteristics are consistent with top of the lithosphere being partially constructed by mafic magmatic rocks. This interpretation is further supported by analysis of the ray coverage or the DWS (Fig. 5e). Although the ray density at all ends of the seismic profiles is gradually reduced with increasing shot distance from the last OBS (Figs. 5c and 5e), the reduction at the west end of the EW profile (Fig. 5f) is considerably greater than at the three other profile ends, which is indicative of a major change in the nature of the lithosphere. This more rapid drop in ray density also coincides in an apparent westward velocity increase at the western limit of the well resolved area (Fig. 9a), but this is an artifact. The inverted velocity model follows the starting velocity

model in areas of low ray coverage (i.e. outside the well resolved area), and in the well resolved section of the western zone seismic velocities are considerably slower than the starting velocity model. This forces a gradual lateral change from the well resolved area. On the contrary, in the east the starting and the average velocity models have similar velocities and no lateral change is observed across the limit of the well resolved area.

In between the eastern and western zones is the central zone, which displays gradual westward changes in the velocities (decreasing; Fig. 9a), velocity anomaly (from low positive to low negative Fig. 9b), and vertical velocity gradient (vertically less variable, Fig. 9c). We interpret this as indicative of a transition from the amagmatic upper lithosphere of the eastern zone to the mafic magmatic rocks toping the lithosphere of the western zone and also likely an indicator of a transitional lithosphere that is heterogeneous in its composition with layers of mafic extrusive and intrusive rocks laterally intertwined with layers of fully and partially serpentinized ultramafic rocks (Fig. 8b).

5.2.3 Anisotropy

We extract 1D velocity-depth functions at the crossing point between the NS and EW velocity profiles (Fig. 10a) to evaluate if there is directional dependence in seismic velocities or seismic anisotropy (Fig. 10). The difference between these two 1D velocity-depth functions is shown in Figure 10b (dashed blue line), and the corresponding anisotropy is shown in Figure 10c. Both velocity functions are nearly coincident for the first 0.5 km dbsf. At greater depth, from ~0.5 to ~2.2 km dbsf, velocities on the EW profile are faster (up to ~5% difference) than on the NS profile. The velocity relationship reverses from ~2.2 to ~6 km dbsf, with the NS profile being faster (up to ~5% difference). At depths greater than 6 km dbsf, the two velocity-depth functions are again nearly coincident.

Figure 10b also compares the difference in the two velocity-depth functions to the standard deviation (SD) estimated for the NS and EW velocity models at their crossing point. The SD-depth functions are similar for both profiles at the crossing point, with most SD values being <±0.1 km/s. The P-wave velocity difference near the function peaks reaches or approaches ±0.4 km/s, which is at least several times greater than the SD of the both velocity models indicating that the difference in velocities we observe falls well within the estimated uncertainty. While some of the differences in velocities at the two crossing profiles may be due to the limitations of modeling wave propagation in 2D, most of the observed differences can be attributed to seismic anisotropy thus rendering our results a useful first-order approximation.

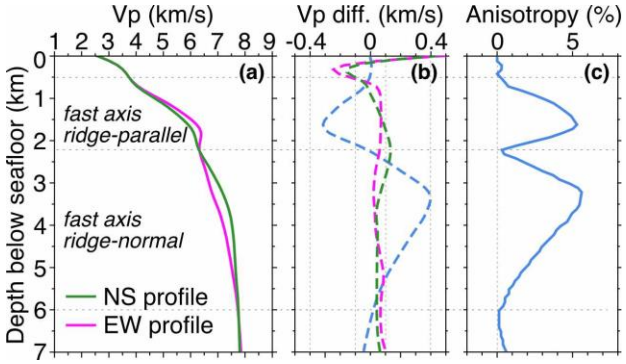

Figure 10. (a) Comparison of the 1D velocity-depth functions extracted from the NS (green) and EW (pink) profiles at their crossing point. (b) Dashed blue line shows the difference between NS and EW velocities presented in (a), and green and pink dashed lines show the standard deviation of the velocities presented in (a) (from Figs. 5b and 5e). (c) Functional fit of % of anisotropy with depth in light blue. The horizontal dashed grey lines in (a, b and c) indicate the depths for the anisotropy consistent with a fast axis aligned in a ridge-parallel direction (~0.5 to ~2.2 km dbsf) and for the anisotropy consistent with a fast axis aligned in a ridge-normal direction (~2.2 to 6 km dbsf).

The velocity differences in the shallower zone (~0.5 to ~2.2 km dbsf) are consistent with the anisotropy reported at other ridges near the spreading axis of 1%–12% at shallow to intermediate depths (0–3 km) and with the fast axis aligned in a ridge-parallel direction (e.g. Seher et al., 2010; Weekly et al., 2014). This anisotropy is associated with the alignment of vertical cracks within the crust in the ridge axis direction (Dunn & Toomey, 2001). Christeson et al. (2019) synthesized the oceanic crustal structure formed at spreading ridges with half-spreading velocities greater than 5 mm/yr from 2D seismic profiles and documented that anisotropy may be restricted to the upper crust in areas near the ridge axis. Cracks induced by stresses related to the footwall exhumation and bending at shallow to intermediate levels both in the footwall and the hanging wall, as well as extensive extensional damage on the hanging wall, have been suggested in our study area (Cannat et al., 2019; Momoh et al., 2017, 2020). Therefore, we suggest the uppermost anisotropy is due to the preferential distribution of cracks parallel or subparallel to the axis at depths from ~0.5 to ~2.2 km dbsf. We expect that the top 0.5 km dbsf are also characterized by axis parallel or subparallel cracks and the resulting anisotropy but, due to the discussed limitations of our data and velocity models, this anisotropy was not possible to resolve.

With greater depth, the increasing lithospheric pressure gradually closes the cracks thus removing the source of the ridge-parallel anisotropy. Serpentinization also diminishes with increasing depth leading to increased ratio of olivine minerals versus serpentine or other alteration minerals, thus generating anisotropy with the ridge-normal fast direction that starts to prevail at ~2.2 km dbsf. Our data can resolve the ridge-normal fast anisotropy to 6 km dbsf, after which the model resolution is insufficient for this purpose. Velocities from 6–~7 km dbsf have diminished resolution and are already influenced by the starting velocity model through smoothing. This uppermost mantle, ridge-normal anisotropy is related to the lattice-preference orientation of olivine minerals in the direction of lithospheric strain (Hess 1964), which is consistent with the near-orthogonal spreading direction attributed to our study area (Cannat et al., 2008), and has been reported for older oceanic crust (e.g. Ismaïl and Mainprice, 1998; VanderBeek et al., 2016).

5.3 Comparison of velocity-depth fields

We compare the average 1D velocities and velocity field envelopes of the NS and EW profiles (Fig. S9) with corresponding results from previously published ridge-normal and ridge-parallel seismic profiles, respectively, at other locations along the SWIR.

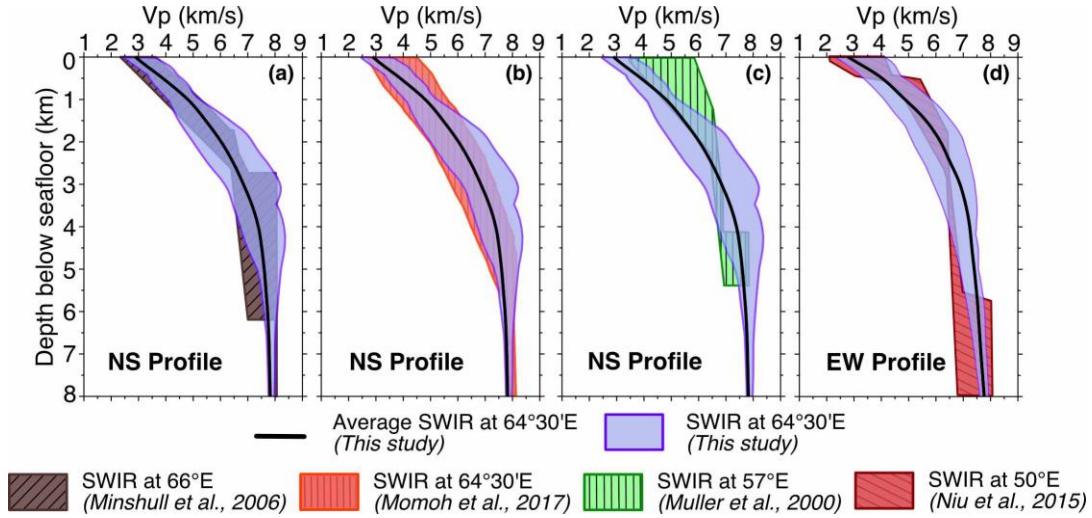

Figure 11. Comparison of the average 1D velocity-depth profiles (thick black line) and 1D velocity-depth fields (light purple areas bounded by dark purple lines) from this study with the velocity fields from earlier studies of the SWIR at the following locations: (a) 66°E (Minshull et al., 2006); (b) 64°30'E (Momoh et al., 2017); (c) 57°E (Muller et al., 2000); and (d) 50°E (Niu et al., 2015). Note that the locations of the earlier work done at 66°, 57° and 50°E are shown in the Figure 1 inset with yellow circle, diamond and star, respectively, while the work done at 64°30'E coincides with our study area.

Figure 11 displays a comparison of our results at 64°30'E with velocity fields from earlier work at the SWIR. From East to West, shown are velocity fields at 66°E (Minshull et al., 2006) (Fig. 11a), 64°30'E (Momoh et al., 2017) (Fig. 11b), 57°E (Muller et al., 2000) (Fig. 11c), and 50°E (Niu et al., 2015) (Fig. 11d).

Our NS profile velocity envelope and that of Momoh et al. (2017) (Fig. 11b), both from 64°30'E, are mostly in general agreement. Momoh et al. (2017) shows little structure with velocities smoothly increasing with depth, from ~2.7 km/s to 4.5 km/s at the seafloor to ~7–8 km/s at 5 km dbsf. The NS velocity model constrains the velocities at the seafloor to a narrower and slower range (~2.5–3.7 km/s), increasing to a similar range by about 1.4 km dbsf, and becoming overall higher for depths up to ~5 km dbsf. Momoh et al.'s (2017) velocities show smooth vertical velocity gradient changes with depth, while the NS velocities indicate a more complex structure for how the velocity gradient changes with depth and show a higher vertical velocity gradient at the top that it is reduced to a lower velocity gradient for depths greater than ~2 km dbsf. While our interpretation is broadly similar to that of Momoh et al. (2017), the NS velocity model has recovered deeper and more detailed velocity information thus providing more constraints on the lithospheric structure. This is likely because the NS profile is longer (150 km vs. 43 km) and has more OBSs (16 vs. 8) than the profiles used by Momoh et al. (2017), resulting in denser and deeper ray coverage with a larger range of source-receiver offsets.

Minshull et al. (2006) at 66°E (Fig. 11a) show velocities at the seafloor ranging from ~2.3–3.5 km/s and increasing at a high vertical velocity gradient up to ~6.4–7 km/s at ~2.7 km dbsf. At depths greater than ~2.7 km dbsf, the velocities increase at a low-velocity gradient and range from ~6.5–7 to 8 km/s. The average velocities for the NS profile fit well with the velocity field of Minshull et al. (2006). The NS velocity field also presents a similar range and vertical gradient for depths up to 1 km dbsf but it has a lower low and a higher high velocity for depths

of 1–3.5 km dbsf. At greater depths, the NS profile velocities are overall higher than the velocities at 66°E. Despite the significant similarities in velocities between the two models, large differences exist on the lithospheric structure interpretation in these two study areas that are only ~150–200 km apart. Minshull et al. (2006) suggested a crustal structure composed of mafic oceanic layers 2 and 3, with a mean crustal thickness of 4.2 km, and constrained the Moho with *PmP* arrivals and complementary gravity data. They interpreted that serpentinized peridotites do not form the dominant lithology in the seismic lower crust and instead they suggested a Layer 3 with a variable thickness (0.5–3 km) governed by melt focusing toward segment centers.

The presence of Segment-8 volcano at ~65°40'E (Cannat et al., 2006; Schlindwein & Schmid, 2016) could explain some of the differences between the two results and interpretations. Velocity structure of Minshull et al. (2006) shows a higher gradient for the top and lower gradient for the bottom of the model than the NS profile, which is consistent with a high-gradient Layer 2 on top of a low-gradient Layer 3, while the SWIR at 64°30'E has a gradual decrease in the vertical velocity gradient consistent with a gradual decrease in serpentinization and pore pressure with depth. However, Minshull et al. (2006) used a layered modeling and inversion procedure constrained by model parametrization of two crustal layers. The wide-angle data were collected on 8 OBSs (~10–30 km spacing) with no coincident MCS data to guide the layered inversion. Therefore, we speculate that a fair amount of variably serpentinized peridotites may be present in the subsurface at the SWIR at 66°E based on the overlap of the NS profile velocity envelope with Minshull et al. (2006) velocities, and that a denser seismic survey followed by first arrival traveltime tomography for a single model layer would provide a better and more detailed comparison.

The SWIR at 57°E (Fig. 11c), across the Atlantic Bank, shows velocities ranging from 3.5 km/s to ~5.8 km/s at the seafloor (Muller et al., 2000). This velocity range gradually narrows to 6.4–6.9 km/s for depths ~2.2–4.1 km dbsf as the vertical velocity gradient decreases. For depths greater than 4.1 km dbsf the velocities range from ~6.8–7.8 km/s. The authors interpreted magmatic oceanic crust composed of layers 2 and 3 on top of the uppermost mantle rocks. The NS profile velocities are overall in disagreement showing slower velocities for depths up to ~2.6 km dbsf and higher velocities for greater depths. We interpret the topmost ~2.6 km dbsf on the NS profile, characterized by lower velocities than those from Muller et al. (2000), to represent fully serpentinized and highly fractured peridotites at the top that gradually transition to ~40% serpentinized peridotites with minor fractures at the bottom. The NS profile velocities continue to increase with increasing depth, though at a reduced gradient, due to continued fracture closure and further diminishing serpentinization. The Moho at the SWIR at 57°E is constrained by *PmP* reflections and gravity modeling, in contrast to our study area where the amagmatic seismic crust lacks any shreds of evidence of a Moho. However, the results from Muller et al. (2000) likely have greater uncertainties than our results since they use only 8 OBSs (~5–15 km spacing) and do not have coincident reflection data, which are used to guide layered modeling and inversion.

The velocity field at the segment center at 50°E (Fig. 11d, Niu et al., 2015) can be divided in 4 sections: (1) top one (0-~0.6 km dbsf), with a mostly moderate gradient and velocities ranging from ~2 km/s to ~4 km/s; (2) a high gradient section underneath (0.6–2.8 km dbsf) with velocities of ~4.4–6.5 km/s; (3) a low gradient section (2.8–5.5 km dbsf) further down with a narrow range of velocities (6.5–7 km/s); and (4) a low gradient section (depth > 5.5 km dbsf) at the bottom with velocities ranging from 6.6 km/s to 8.1 km/s. The NS profile velocities are mostly in agreement within the top section, lower than velocities of Niu et al. (2015) in the

top part and in agreement with the bottom part of the second section, are significantly higher in the third section, and somewhat higher in the fourth section. Niu et al. (2015) interpreted layers 2A, 2B, and 3 overlying the uppermost mantle. The investigated segment center at 50°E has an anomalously thick crust, ranging from ~5.5 km to 10.2 km, and a robust and well-imaged axial magma chamber (Niu et al., 2015; Jian et al., 2016, 2017). This interpretation is consistent with a magma-rich spreading center and, as such, it differs from magma-starved spreading interpreted at 64°30'E.

6 Conclusions

We constrain tomographic velocity structure across- and along-axis the ultraslow-spreading SWIR at 64°30'E by inverting first arrivals from two ~150-km-long orthogonal wide-angle OBS profiles. Our major findings and conclusions are the following:

1. About 75% of the investigated uppermost lithosphere appears to be composed of highly fractured and fully serpentinized peridotites at the top, with a gradual decrease in pore space volume and serpentinization degree to unaltered peridotites at depth. Key evidence for this are seismic velocities that increase rapidly with depth, changing from 3–4 km/s at the seafloor to 7 km/s at depths ranging from 1.5–6 km dbsf, much lower vertical velocity gradient for velocities >7 km/s that gradually reduces with increasing depth, and no distinct and seismically well-characterized Moho observable in the data.

2. A system of detachment faults is imaged in the subsurface for the first time in our study area by the profile that crosses the ridge axis. We interpret a sharp lateral change (horizontal gradient ~1 s^{-1}) in velocities, switch in polarity of the largest velocity anomaly, from 1.5 km/s to -1.5 km/s, and high vertical gradient (~2 s^{-1}) in the velocities coincident with the shallow section (top 2 km) of the highest topographic feature as the seismic expression of an active axial detachment fault. Five abandoned detachment faults are also identified based on anomalously high velocities and vertical gradients that characterize the footwalls on all identified detachment faults, with the opposite characterizing the hanging walls. Serpentinization across-axis is controlled by the longevity of detachments and fault block movement, with longer-lived faults showing deeper serpentinization extent and footwalls showing less pervasive serpentinization due to continuous exhumation.

3. Comparison of the 1D velocity-depth functions at their crossing point between the two orthogonal profiles suggests an up to 5% ridge-parallel fast-axis anisotropy from ~0.5 to ~2.2 km dbsf attributed to the preferential distribution of cracks parallel to the ridge, and a similar magnitude but reversed polarity ridge-normal fast-axis anisotropy at >~2.2 km dbsf that we attribute to the lattice-preference orientation of olivine minerals in the less serpentinized peridotites.

4. Upper lithospheric composition along the western half of the axis-parallel profile seems to transition over a distance of ~10 km from the variably serpentinized peridotites domains in the East to predominately mafic magmatic domains in the West. The exhumed mantle domains show high and laterally variable seismic velocities at shallow depths, reaching 4–4.5 km/s within the first 0.5 km dbsf and 7 km/s at depths 2–3.5 km dbsf, a high vertical velocity gradient of 1–2 s^{-1}, and an overall positive velocity anomaly (up to 0.5-1 km/s). The mafic domains show sharply lower seismic velocities that reach

3.5 km/s at 0.5 km dbsf and 7 km/s only at 4–5.3 km dbsf, a moderate to low and smoother vertical velocity gradient of 0.5–1 s^{-1}, and a large negative velocity anomaly of -1.5–-1 km/s. We suggest that the change in the seafloor accretion mode is propelled by a westward increase in melt supply.

5. Comparison of velocity structure from our results at the ultraslow-spreading SWIR at 64°30'E with the velocity structure elsewhere at the SWIR has shown an overall agreement of our results with studies at amagmatic segments, a disagreement with identified anomalously magma-rich segments, and mixed results for magma-starved segments, such as the SWIR at 66° and 57° E. This work has also demonstrated the challenges in carrying out meaningful velocity structure comparisons when the data resolution and techniques used to determine the velocities are not the same (e.g. layered modeling vs. tomography).

Acknowledgments and data

AC was supported by "la Caixa" Foundation [Scholarship LCF/BQ/AN15/10380004], NSERC CREATE TOSST (NSERC Collaborative Research and Training Experience for the Transatlantic Ocean System Science and Technology), and an NSERC Discovery Grant to MRN. AC also thanks HOSST and GEOMAR for their support and training experience during her research exchange. The authors are grateful to the Flotte Océanographique Française (FOF) and an NSERC Ship Time grants that funded the SISMOSMOOTH cruise, and CNRS-INSU Tellus, ANR Rift2Ridge NT09-48546 and RidgeFactory-Slow 18-CE01-0002-01 for providing support for the cruise. We also thank Captain Thierry Dudouit (CMO-CGM) and the crew of the R/V Marion-Dufresne, and Erwan Nedelec and Jean-Charles Guedes (Genavir) for the seismic deployment. Raw data are available on request from SISMER (https://doi.org/10.17600/14003300). Velocity models are available on request from the National Facility for Seismic Imaging (www.nfsi.ca). Figures were produced using the Generic Mapping Tools (GMT) software (Wessel and Smith, 1998).

References

Aghaei, O., Nedimović, M.R., Carton, H., Carbotte, S.M., Canales, J.P., & Mutter, J.C. (2014). Crustal thickness and Moho character of the fast-spreading East Pacific Rise from 9° 42′ N to 9° 57′ N from poststack-migrated 3-D MCS data. *Geochemistry, Geophysics, Geosystems*, *15*(3), 634-657. https://doi.org/10.1002/2013GC005069

Alt, J., Bach, W., Edwards, K., Frost, R., Früh-Green, G., Godard, M., et al. (2009). Drilling in Serpentine Sea. In *White Paper ''Serpentine Sea'' presented at the INVEST conference, Bremen*, 23-25.

Argus, D.F., Gordon, R.G., & DeMets, C. (2011). Geologically current motion of 56 plates relative to the no-net-rotation reference frame. *Geochemistry, Geophysics, Geosystems, 12*(11).

Arnulf, A.F., Harding, A.J., Singh, S.C., Kent, G.M. & Crawford, W. (2012). Fine-scale velocity structure of upper oceanic crust from full waveform inversion of downward continued seismic reflection data at the Lucky Strike Volcano, Mid-Atlantic Ridge. *Geophysical Research Letters*, *39*(8).

946 Barclay, A.H., Toomey, D.R., & Solomon, S.C. (1998). Seismic structure and crustal magmatism
947 at the Mid-Atlantic Ridge, 35° N. *Journal of Geophysical Research: Solid Earth*, *103*(B8),
948 17827-17844.

949 Berge, P.A., Fryer, G.J., & Wilkens, R.H. (1992). Velocity-porosity relationships in the upper
950 oceanic crust: Theoretical considerations. *Journal of Geophysical Research: Solid Earth*,
951 *97*(B11), 15239-15254.

952 Bird, P. (2003). An updated digital model of plate boundaries. *Geochemistry, Geophysics,*
953 *Geosystems, 4*(3).

954 Bickert, M., Lavier, L., & Cannat, M. (2020). How do detachment faults form at ultraslow mid-
955 ocean ridges in a thick axial lithosphere? *Earth and Planetary Science Letters*, *533*.
956 https://doi.org/10.1016/j.epsl.2019.116048

957 Blackman, D.K., Karson, J.A., Kelley, D.S., Cann, J.R., Früh-Green, G.L., Gee, J.S., et al.
958 (2002). Geology of the Atlantis Massif (Mid-Atlantic Ridge, 30 N): Implications for the
959 evolution of an ultramafic oceanic core complex. *Marine Geophysical Researches*, *23*(5), 443-
960 469.

961 Boulahanis, B., Carbotte, S.M., Huybers, P.J., Nedimović, M.R., Aghaei, O., Canales, J.P., &
962 Langmuir, C.H. (2020). Do sea level variations influence mid-ocean ridge magma supply? A test
963 using crustal thickness and bathymetry data from the East Pacific Rise. *Earth and Planetary*
964 *Science Letters*, *535*. https://doi.org/10.1016/j.epsl.2020.116121

965 Bratt, S. R., & Purdy, G. M. (1984). Structure and variability of oceanic crust on the flanks of the
966 East Pacific Rise between 11° and 13°N. *Journal of Geophysical Research: Solid Earth*, *89*,
967 6111–6125.

968 Canales, J.P., Detrick, R. S., Toomey, D. R., & Wilcock, W. S. D. (2003). Segment-scale
969 variations in the crustal structure of 150-300 kyr old fast spreading oceanic crust (East Pacific
970 rise, 8°15'N-10°5'N) from wide-angle seismic refraction profiles. *Geophysical Journal*
971 *International*, *152*(3), 766–794. https://doi.org/10.1046/j.1365-246X.2003.01885.x

972 Canales, J.P., Detrick, R.S., Lin, J., Collins, J. A., & Toomey, D.R. (2000). Crustal and upper
973 mantle seismic structure beneath the rift. *Journal of Geophysical Research*, *105*(B2), 2699–2719.

974 Canales, J.P., Tucholke, B.E. & Collins, J.A. (2004). Seismic reflection imaging of an oceanic
975 detachment fault: Atlantis megamullion (Mid-Atlantic Ridge, 30 10′ N). *Earth and Planetary*
976 *Science Letters, 222*(2), 543-560.

977 Canales, J.P., Detrick, R.S., Carbotte, S.M., Kent, G.M., Diebold, J.B., Harding, A., et al. (2005).
978 Upper crustal structure and axial topography at intermediate spreading ridges: Seismic
979 constraints from the southern Juan de Fuca Ridge. *Journal of Geophysical Research: Solid*
980 *Earth, 110*(B12).

981 Cann, J.R., Blackman, D.K., Smith, D.K., McAllister, E., Janssen, B., Mello. S., et al. (1997).
982 Corrugated slip surfaces formed at ridge–transform intersections on the Mid-Atlantic Ridge.
983 *Nature 385*, 329–332. https://doi.org/10.1038/385329a0

984 Cannat, M. (1993). Emplacement of mantle rocks in the seafloor at mid-ocean ridges. *Journal of*
985 *Geophysical Research: Solid Earth, 98*(B3), 4163-4172.

Cannat, M., Céline, R.J., & Fujimoto, H. (2003). Melt supply variations to a magma-poor ultra-slow spreading ridge (Southwest Indian Ridge 61° to 69°E). *Geochemistry, Geophysics, Geosystems*, *4*(8), 1–21. https://doi.org/10.1029/2002GC000480

Cannat, M., Sauter, D., Mendel, V., Ruellan, E., Okino, K., Escartin, J., et al. (2006). Modes of seafloor generation at a melt-poor ultraslow-spreading ridge. *Geology*, *34*(7), 605–608. https://doi.org/10.1130/G22486.1

Cannat, M., Sauter, D., Bezos, A., Meyzen, C., Humler, E., & Le Rigoleur, M. (2008). Spreading rate, spreading obliquity, and melt supply at the ultraslow spreading Southwest Indian Ridge. *Geochemistry, Geophysics, Geosystems*, *9*(4), 1–26. https://doi.org/10.1029/2007GC001676

Cannat, M., Sauter, D., Lavier, L., Bickert, M., Momoh, E., & Leroy, S. (2019). On spreading modes and magma supply at slow and ultraslow mid-ocean ridges. *Earth and Planetary Science Letters*, *519*, 223–233. https://doi.org/10.1016/j.epsl.2019.05.012

Carbotte, S.M. & Scheirer, D.S. (2004). Variability of ocean crustal structure created along the global mid-ocean ridge. *Hydrogeology of the oceanic lithosphere*, 59-107.

Carbotte, S.M., Detrick, R.S., Harding, A., Canales, J.P., Babcock, J., Kent, G., et al. (2006). Rift topography linked to magmatism at the intermediate spreading Juan de Fuca Ridge. *Geology, 34*(3), 209-212.

Carbotte, S.M., Nedimović, M.R., Canales, J.P., Kent, G.M., Harding, A.J. & Marjanović, M. (2008). Variable crustal structure along the Juan de Fuca Ridge: Influence of on-axis hot spots and absolute plate motions. *Geochemistry, Geophysics, Geosystems, 9*(8).

Carlson, R.L. & Miller, D.J. (1997). A new assessment of the abundance of serpentinite in the oceanic crust. *Geophysical Research Letters, 24*(4), 457-460.

Carlson, R.L., & Miller, D.J. (2003). Mantle wedge water contents estimated from seismic velocities in partially serpentinized peridotites. *Geophysical Research Letters*, *30*(5). https://doi.org/10.1029/2002gl016600

Carter, D.J.T. (1980). Echosounding correction tables (formerly Matthews tables), Hydrographic Department, Ministry of Defenoe, Taunton, UK.

Chen, Y.J. (1992). Oceanic crustal thickness versus spreading rate. *Geophysical Research Letters*, *19*(8), 753-756.

Christensen, N.I. (1972). The abundance of serpentinites in the oceanic crust. *The Journal of Geology, 80*(6), 709-719.

Christensen, N.I. & Salisbury, M.H. (1975). Structure and constitution of the lower oceanic crust. *Reviews of Geophysics, 13*(1), 57-86.

Christensen, N.I. (1978). Ophiolites, seismic velocities and oceanic crustal structure. *Tectonophysics*, *47*(1-2), 131-157.

Christensen, N.I. & Smewing, J.D. (1981). Geology and seismic structure of the northern section of the Oman ophiolite. *Journal of Geophysical Research: Solid Earth, 86*(B4), 2545-2555.

Christensen, N.I. (1996). Poisson's ratio and crustal seismology. *Journal of Geophysical Research: Solid Earth, 101*(B2), 3139-3156.

1025 Christeson, G.L., McIntosh, K.D., & Karson, J.A. (2007). Inconsistent correlation of seismic
1026 layer 2a and lava layer thickness in oceanic crust. *Nature*, *445*(7126), 418–421.

1027 Christeson, G.L., Goff, J.A., & Reece, R.S. (2019). Synthesis of oceanic crustal structure from
1028 two-dimensional seismic profiles. *Reviews of Geophysics, 57*, 504– 529.
1029 https://doi.org/10.1029/2019RG000641

1030 Christeson, G.L., Reece, R.S., Kardell, D.A., Estep, J.D., Fedotova, A. & Goff, J.A. (2020).
1031 South Atlantic Transect: Variations in Oceanic Crustal Structure at 31° S. *Geochemistry,*
1032 *Geophysics, Geosystems, 21*(7).https://doi.org/10.1038/nature05517

1033 deMartin, B.J., Sohn, R.A., Canales, J.P. & Humphris, S.E. (2007), Kinematics and geometry of
1034 active detachment faulting beneath the Trans-Atlantic Geotraverse (TAG) hydrothermal field on
1035 the Mid-Atlantic Ridge. *Geology*, *35*, 711– 714.

1036 Dannowski, A., Grevemeyer, I., Ranero, C.R., Ceuleneer, G., Maia, M., Morgan, J.P. & Gente,
1037 P. (2010). Seismic structure of an oceanic core complex at the Mid-Atlantic Ridge, 22 19′ N.
1038 *Journal of Geophysical Research: Solid Earth, 115*(B7).

1039 Detrick, R.S., Harding, A.J., Kent, G.M., Orcutt, J.A., Mutter, J.C. & Buhl, P. (1993). Seismic
1040 structure of the southern East Pacific Rise. *Science, 259*(5094), 499-503.

1041 Dick, H.J.B., Lin, J., & Schouten, H. (2003). An ultraslow-spreading class of ocean ridge.
1042 *Nature*, *426*(6965), 405–412. https://doi.org/10.1038/nature02128

1043 Dick, H.J.B., Tivey, M.A. & Tucholke, B.E. (2008). Plutonic foundation of a slow-spreading
1044 ridge segment: Oceanic core complex at Kane Megamullion, 23 30′ N, 45 20′ W. *Geochemistry,*
1045 *Geophysics, Geosystems, 9*(5).

1046 Dick, H.J.B., Lissenberg, C.J., & Warren, J.M. (2010). Mantle Melting, Melt Transport, and
1047 Delivery Beneath a Slow-Spreading Ridge: The Paleo-MAR from 23°15′N to 23°45′N. *Journal*
1048 *of Petrology*, *51*(1-2), 425–467. https://doi.org/10.1093/petrology/egp088

1049 Dick, H.J.B., Macleod, C.J., Blum, P., Abe, N., Blackman, D.K., Bowles, J.A., et al. (2019).
1050 Dynamic accretion beneath a slow-spreading ridge segment: IODP Hole 1473A and the Atlantis
1051 Bank Oceanic Core Complex. *Journal of Geophysical Research: Solid Earth*, *124*(12), 12631-
1052 12659.

1053 Dunn, R.A., & Toomey, D.R. (2001). Crack-induced seismic anisotropy in the oceanic crust
1054 across the East Pacific Rise (9°30'N). *Earth and Planetary Science Letters*, *189*(1–2), 9–17.
1055 https://doi.org/10.1016/S0012-821X(01)00353-3

1056 Escartín, J., Mével, C., MacLeod, C.J. & McCaig, A.M. (2003). Constraints on deformation
1057 conditions and the origin of oceanic detachments: The Mid-Atlantic Ridge core complex at 15
1058 45′ N. *Geochemistry, Geophysics, Geosystems, 4*(8).

1059 Escartín, J., Smith, D.K., Cann, J., Schouten, H., Langmuir, C.H. & Escrig, S. (2008). Central
1060 role of detachment faults in accretion of slow-spreading oceanic lithosphere. *Nature, 455*(7214),
1061 790-794.

1062 Escartín, J. & Canales, J. P., (2011), Detachments in Oceanic Lithosphere: Deformation,
1063 Magmatism, Fluid Flow, and Ecosystems. *Eos Trans. AGU, 92(4),* 31.

1064 Estep, J., Reece, R., Kardell, D.A., Christeson, G.L. & Carlson, R.L. (2019). Seismic layer 2A:
1065 Evolution and thickness from 0-to 70-Ma crust in the slow-intermediate spreading South
1066 Atlantic. *Journal of Geophysical Research: Solid Earth, 124*(8), 7633-7651.

1067 Ewing, J. & Ewing, M. (1959). Seismic-refraction measurements in the Atlantic Ocean basins, in
1068 the Mediterranean Sea, on the Mid-Atlantic Ridge, and in the Norwegian Sea. *Geological Society*
1069 *of America Bulletin, 70*(3), 291-318.

1070 Früh-Green, G.L., Orcutt, B.N., Rouméjon, S., Lilley, M.D., Morono, Y., Cotterill, C., et al.
1071 (2018). Magmatism, serpentinization and life: Insights through drilling the Atlantis Massif
1072 (IODP Expedition 357). *Lithos*, *323*, 137-155.

1073 Fujie, G., Kasahara, J., Murase, K., Mochizuki, K. & Kaneda, Y. (2008). Interactive analysis
1074 tools for the wide-angle seismic data for crustal structure study (Technical Report). *Exploration*
1075 *Geophysics*, *39*(1), 26-33.

1076 Grevemeyer, I., Weigel, W., & Jennrich, C. (1998). Structure and ageing of oceanic crust at 14 °
1077 S on the East Pacific Rise. *Geophysical Journal International*, *135*, 573–584.

1078 Grevemeyer, I., Hayman, N. W., Peirce, C., Schwardt, M., Avendonk, H. J. A. Van, Dannowski,
1079 A., & Papenberg, C. (2018b). exhumation at an ultraslow-spreading centre. *Nature Geoscience*,
1080 *11*, 444–449. https://doi.org/10.1038/s41561-018-0124-6

1081 Grevemeyer, I., Ranero, C. R., & Ivandic, M. (2018a). Structure of oceanic crust and
1082 serpentinization at subduction trenches. *Geosphere*, *14*(2), 395–418.
1083 https://doi.org/10.1130/GES01537.1

1084 Han, S., Carbotte, S.M., Carton, H., Mutter, J.C., Aghaei, O., Nedimović, M.R. & Canales, J.P.
1085 (2014). Architecture of on-and off-axis magma bodies at EPR 9 37–40′ N and implications for
1086 oceanic crustal accretion. *Earth and Planetary Science Letters, 390*, 31-44.

1087 Hess, H.H. (1964). Seismic anisotropy of the uppermost mantle under oceans. *Nature,*
1088 *203*(4945),629-631.

1089 Horning, G., Canales, J.P., Carbotte, S. M., Han, S., Carton, H., Nedimović, M.R., & Van
1090 Keken, P.E. (2016). A 2-D tomographic model of the Juan de Fuca plate from accretion at axial
1091 seamount to subduction at the Cascadia margin from an active source ocean bottom seismometer
1092 survey. *Journal of Geophysical Research: Solid Earth*, *121*(8), 5859-5879.
1093 https://doi.org/10.1002/2016JB013228

1094 Houtz, R., & Ewing, J. (1976). Upper crustal structure as a function of plate age. *Journal of*
1095 *Geophysical Research, 81*(14), 2490-2498.

1096 Ildefonse, B., Blackman, D.K., John, B.E., Ohara, Y., Miller, D.J. & MacLeod, C.J. (2007).
1097 Oceanic core complexes and crustal accretion at slow-spreading ridges. *Geology, 35*(7), 623-626.

1098 Ismaïl, W.B., & Mainprice, D. (1998). An olivine fabric database: an overview of upper mantle
1099 fabrics and seismic anisotropy. *Tectonophysics, 296*(1–2), 145–157.
1100 https://doi.org/10.1016/S0040-1951(98)00141-3

1101 Jian, H., Chen, Y.J., Singh, S.C., Li, J., Zhao, M., Ruan, A., & Qiu, X. (2016). Seismic structure
1102 and magmatic construction of crust at the ultraslow-spreading Southwest Indian Ridge at
1103 50°28'E. *Journal of Geophysical Research : Solid Earth*, *121*, 18–42.
1104 https://doi.org/10.1002/2016JB013377

Jian, H., Singh, S. C., Chen, Y. J., & Li, J. (2017). Evidence of an axial magma chamber beneath the ultraslow-spreading Southwest Indian Ridge. *Geology*, *45*(2), 143–146. https://doi.org/10.1130/G38356.1

Jokat, W., & Schmidt-Aursch, M. C. (2007). Geophysical characteristics of the ultraslow spreading Gakkel Ridge, Arctic Ocean. *Geophysical Journal International*, *168*(3), 983–998. https://doi.org/10.1111/j.1365-246X.2006.03278.x

Kandilarov, A., Landa, H., Mjelde, R., Pedersen, R. B., Okino, K., & Murai, Y. (2010). Crustal structure of the ultra-slow spreading Knipovich Ridge, North Atlantic, along a presumed ridge segment center. *Marine Geophysical Research*, *31*(3), 173–195. https://doi.org/10.1007/s11001-010-9095-8

Kandilarov, A., Mjelde, R., Okino, K. & Murai, Y. (2008). Crustal structure of the ultra-slow spreading Knipovich Ridge, North Atlantic, along a presumed amagmatic portion of oceanic crustal formation. *Marine Geophysical Researches, 29(2)*, 109-134.

Kardell, D.A., Christeson, G.L., Estep, J.D., Reece, R.S. & Carlson, R.L. (2019). Long-lasting evolution of layer 2A in the Western South Atlantic: Evidence for low-temperature hydrothermal circulation in old oceanic crust. *Journal of Geophysical Research: Solid Earth*, *124*(3), 2252-2273.

Kelley, D.S., Karson, J.A., Früh-Green, G.L., Yoerger, D.R., Shank, T.M., Butterfield, D.A., et al. (2005). A serpentinite-hosted ecosystem: The Lost City Hydrothermal Field, *Science*, *307*(5714), 1428– 1434. https://doi.org/10.1126/science.1102556

Klingelhöfer, F., Géli, L., Matias, L., Steinsland, N., & Mohr, J. (2000). Crustal structure of a super-slow spreading centre: A seismic refraction study of Mohns Ridge, 72°N. *Geophysical Journal International*, *141*(2), 509–526. https://doi.org/10.1046/j.1365-246X.2000.00098.x

Korenaga, J., Holbrook, W.S., Kent, G.M., Kelemen, P.B., Detrick, R.S., Larsen, H.C., et al. (2000). Crustal structure of the southeast Greenland margin from joint refraction and reflection seismic tomography. *Journal of Geophysical Research*, *105*, 21591. https://doi.org/10.1029/2000JB900188

Kreemer, C., Blewitt, G., & Klein C.E. (2014). A geodetic plate motion and Global Strain Rate Model. *Geochemistry, Geophysics, Geosystems*, 3849–3889. https://doi.org/10.1002/2014GC005407

Lavier, L.L., Buck, W.R., & Poliakov, N.B. (1999). Self-consistent rolling-hinge model for the evolution of large-offset low-angle normal faults. *Geology, 27*, 1127–1130, doi:10.1130/0091-7613(1999)027<1127:SCRHMF>2.3.CO;2.

Leroy S., & Cannat, M. (2014). MD 199/SISMO-SMOOTH cruise, Marion Dufresne R/V. https://doi.org/10.17600/14003300

Leroy, S., Cannat, M., Momoh, E., Singh, S., Watremez, L., Sauter, D., et al. (2015). Anatomy of ultra-slow spreading Southwest Indian Ridge: The 2014 SISMOSMOOTH cruise. Abstract V21A-3027 Paper presented at the 2015 AGU, San Francisco, CA, 14–18 Dec.

Li, J., Jian, H., Chen, Y. J., Singh, S. C., Ruan, A., Qiu, X., et al. (2015). Seismic observation of an extremely magmatic accretion at the ultraslow spreading Southwest Indian Ridge. *Geophysical Research Letters*, *42*(8), 2656–2663. https://doi.org/10.1002/2014GL062521

Lin, J., Purdy, G.M., Schouten, H. Sempere, J.C., & Zervas, C. (1990). Evidence from gravity data for focused magmatic accretion along the Mid-Atlantic Ridge. *Nature 344*, 627–632. https://doi.org/10.1038/344627a0

Mével, C. (2003). Serpentinization of abyssal peridotites at mid-ocean. *Comptes Rendus Geoscience*, *335*(10–11), 825–852. https://doi.org/10.1016/j.crte.2003.08.006

Miller, D.J. & Christensen, N.I. (1997). Seismic velocities of lower crustal and upper mantle rocks from the slow-spreading Mid-Atlantic Ridge, south of the Kane Transform Zone (MARK). *In Proceedings-Ocean Drilling Program Scientific Results*, 437-456. National Science Foundation.

Minshull, T.A., Muller, M.R., Robinson, C.J., White, R.S., & Bickle, M.J. (1998). Is the oceanic Moho a serpentinization front? *Geological Society, London, Special Publications*, *148*(1), 71–80. https://doi.org/10.1144/GSL.SP.1998.148.01.05

Minshull, T.A., Muller, M.R., & White, R.S. (2006). Crustal structure of the Southwest Indian Ridge at 66°E: Seismic constraints. *Geophysical Journal International*, *166*(1), 135–147. https://doi.org/10.1111/j.1365-246X.2006.03001.x

Momoh, E., Cannat, M., Watremez, L., Leroy, S., & Singh, S. C. (2017). Quasi-3-D Seismic Reflection Imaging and Wide-Angle Velocity Structure of Nearly Amagmatic Oceanic Lithosphere at the Ultraslow-Spreading Southwest Indian Ridge. *Journal of Geophysical Research: Solid Earth*, *122*(12), 9511–9533. https://doi.org/10.1002/2017JB014754

Momoh, E., Cannat, M., & Leroy, S. (2020). Internal Structure of the Oceanic Lithosphere at a Melt-Starved Ultraslow-Spreading Mid-Ocean Ridge: Insights From 2-D Seismic Data. *Geochemistry, Geophysics, Geosystems*, *21*(2). https://doi.org/10.1029/2019GC008540

Moser T.J. (1991). Shortest path calculation of seismic rays. *Geophysics, 56,* 9–159. https://doi.org/10.1190/1.1442958

Moser T.J., Van Eck T., & Nolet G. (1992). Hypocenter determination in strongly heterogeneous earth models using the shortest path method. *Journal of Geophysical Research: Solid Earth, 97*, 6563–6572. https://doi.org/10.1190/1.1442958.

Muller, M.R., Robinson, C.J., Minshull, T.A., White, R.S., & Bickle, M.J. (1997). Thin crust beneath Ocean Drilling Program Borehole 735B at the Southwest Indian Ridge? *Earth and Planetary Science Letters, 148*(1–2), 93–107. http://dx.doi.org/10.1016/S0012-821X(97)00030-7

Muller, M.R., Minshull, T.A. & White, R.S. (1999). Segmentation and melt supply at the Southwest Indian Ridge. *Geology, 27*(10), 867-870.

Muller, M.R., Minshull, T.A., & White, R.S. (2000). Crustal structure of the Southwest Indian Ridge at the Atlantis II Fracture Zone. *Journal of Geophyscial Research*, *105*(B11), 25809 – 25828.

Müller, R.D., Sdrolias, M., Gaina, C., & Roest, W.R. (2008). Age, spreading rates, and spreading asymmetry of the world's ocean crust. *Geochemistry, Geophysics, Geosystems*, *9*(4), 1–19. https://doi.org/10.1029/2007GC001743

Nedimović, M.R., Carbotte, S.M., Harding, A.J., Detrick, R.S., Canales, J.P., Diebold, J.B., et al. (2005). Frozen magma lenses below the oceanic crust. *Nature, 436*(7054), 1149-1152.

Nedimović, M.R., Carbotte, S.M., Diebold, J.B., Harding, A.J., Canales, J.P., & Kent, G.M. (2008). Upper crustal evolution across the Juan de Fuca ridge flanks. *Geochemistry, Geophysics, Geosystems*, *9*(9). https://doi.org/10.1029/2008GC002085

Newman, K.R., Nedimović, M.R., Canales, J.P. & Carbotte, S.M. (2011). Evolution of seismic layer 2B across the Juan de Fuca Ridge from hydrophone streamer 2-D traveltime tomography. *Geochemistry, Geophysics, Geosystems, 12*(5).

Niu, X., Ruan, A., Li, J., Minshull, T.A., Sauter, D., Wu, Z., et al. (2015), Along-axis variation in crustal thickness at the ultraslow spreading Southwest Indian Ridge (50°E) from a wide-angle seismic experiment, *Geochemistry, Geophysics, Geosystems*, *16*, 468– 485, doi:10.1002/2014GC005645

Papazachos C., & Nolet G. (1997). P and S deep velocity structure of the Hellenic area obtained by robust nonlinear inversion of travel times. *Journal of Geophysical Research: Solid Earth, 102*(B4), 8349–8367. doi: https://doi.org/10.1029/96JB03730.

Parnell-Turner, R., Sohn, R.A., Peirce, C., Reston, T.J., MacLeod, C.J., Searle, R.C., & Simão, N.M. (2017). Oceanic detachment faults generate compression in extension. *Geology, 45*, 923–926. https://doi.org/10.1130/G39232.1

Peterson, J.J., Fox, P.J., & Schreiber, E. (1974). Newfoundland ophiolites and the geology of the oceanic layer. *Nature*, *247*(5438), 194-196.

Raitt, R.W. (1963). The crustal rocks. *The Sea*, vol. 3, 85–102. Edited by M. N. Hill. Wiley Interscience, New York.

Reston, T., & McDermott, K.G. (2011). Successive detachment faults and mantle unroofing at magma-poor rifted margins. *Geology*, *39*(11), 1071-1074.

Reston, T. (2018). Flipping detachments: The kinematics of ultraslow spreading ridges. *Earth and Planetary Science Letters*, *503*, 144–157. https://doi.org/10.1016/j.epsl.2018.09.032

Rouméjon, S., Cannat, M., Agrinier, P., Godard, M., & Andreani, M. (2014). Serpentinization and fluid pathways in tectonically exhumed peridotites from the southwest Indian ridge (62-65°E). *Journal of Petrology*, *56*(4), 703–734. https://doi.org/10.1093/petrology/egv014

Sauter, D., & Cannat, M. (2010). The Ultraslow Spreading Southwest Indian Ridge. *Diversity of Hydrothermal Systems on Slow Spreading Ocean Ridges*, (November), 153–173. https://doi.org/10.1029/2008GM000843

Sauter, D., Cannat, M., & Mendel, V. (2008). Magnetization of 0-26.5 Ma seafloor at the ultraslow spreading Southwest Indian Ridge, 61°-67°E. *Geochemistry, Geophysics, Geosystems*, *9*(4), 1–23. https://doi.org/10.1029/2007GC001764

Sauter, D., Cannat, M., Rouméjon, S., Andreani, M., Birot, D., Bronner, A., et al. (2013). Continuous exhumation of mantle-derived rocks at the Southwest Indian Ridge for 11 million years. *Nature Geoscience*, *6*(4), 314–320. https://doi.org/10.1038/ngeo1771

Schlindwein, V. & Schmid, F. (2016). Mid-ocean-ridge seismicity reveals extreme types of ocean lithosphere. *Nature*, *535*(7611), 276–279. https://doi.org/10.1038/nature18277

Schrenk, M.O., Kelley, D.S., Bolton, S.A., & Baross, J.A. (2004). Low archaeal diversity linked to subseafloor geochemical processes at the Lost City Hydrothermal Field, Mid-Atlantic Ridge. *Environmental Microbiology*, *6*(10), 1086-1095.

Seher, T., Crawford, W.C., Singh, S.C., Cannat, M., Combier, V., & Dusunur, D. (2010). Crustal velocity structure of the Lucky Strike segment of the Mid-Atlantic Ridge at 37 N from seismic refraction measurements. *Journal of Geophysical Research: Solid Earth, 115*(B3).

Seyler, M., Cannat, M., & Mével, C. (2003). Evidence for major-element heterogeneity in the mantle source of abyssal peridotites from the Southwest Indian Ridge (52° to 68°E). *Geochemistry, Geophysics, Geosystems*, *4*(2). https://doi.org/10.1029/2002GC000305

Smith, D.K., Cann, J.R., & Escartín, J. (2006). Widespread active detachment faulting and core complex formation near 13°N on the Mid-Atlantic Ridge. *Nature, 442*(7101), 440-443.

Talwani, M., Le Pichon, X., & Ewing, M. (1965). Crustal structure of the mid-ocean ridges: 2. Computed model from gravity and seismic refraction data. *Journal of Geophysical Research, 70*(2), 341-352.

Talwani, M., Windisch, C.C., & Langseth Jr, M.G. (1971). Reykjanes ridge crest: A detailed geophysical study. *Journal of Geophysical Research, 76*(2), 473-517.

Tarantola, A. (1987). Inversion of travel times and seismic waveforms. *Seismic tomography*, 135-157.

Toomey, D.R., & Foulger, G.R. (1989). Tomographic inversion of local earthquake data from the Hengill-Grensdalur central volcano complex, Iceland. *Journal of Geophysical Research: Solid Earth, 94*(B12), 17497-17510.

Tucholke, B.E., & Lin, J. (1994). A geological model for the structure of ridge segments in slow spreading ocean crust. *Journal of Geophysical Research: Solid Earth, 99*(B6), 11937-11958.

Tucholke, B.E., Lin, J., & Kleinrock, M.C. (1998). Megamullions and mullion structure defining oceanic metamorphic core complexes on the Mid-Atlantic Ridge. *Journal of Geophysical Research: Solid Earth*, *103*(B5), pp.9857-9866.

Van Avendonk, H.J.A., Harding, A.J., Orcutt, J.A., & McClain, J.S. (1998). A two-dimensional tomographic study of the Clipperton transform fault. *Journal of Geophysical Research: Solid Earth, 103*, 17885–17899. doi: https://doi.org/10.1029/98JB00904

Van Avendonk, H.J.A., Hayman, N.W., Harding, J.L., Grevemeyer, I., Peirce, C., & Dannowski, A. (2017). Seismic structure and segmentation of the axial valley of the Mid-Cayman Spreading Center. *Geochemistry, Geophysics, Geosystems*, 1–13. https://doi.org/10.1002/2017GC006873

VanderBeek, B.P., Toomey, D.R., Hooft, E.E.E., & Wilcock, W.S.D. (2016). Segmentation of mid-ocean ridges attributed to oblique mantle divergence. *Nature Geosciences, 9*, 636–642. https://doi.org/10.1038/ngeo2745

Vera, E.E., & Diebold, J.B. (1994). Seismic imaging of oceanic layer 2A between 9°30'N and 10°N on the East Pacific Rise from two-ship wide-aperture profiles. *Journal of Geophysical Research*, *99*(B2), 3031–3041. https://doi.org/10.1029/93JB02107

Watremez, L., Lau, H.K.W., Nedimović, M.R., & Louden, K.E. (2015). Traveltime tomography of a dense wide-angle profile across Orphan Basin. *Geophysics*, *80*(3), B69–B82. https://doi.org/10.1190/geo2014-0377.1

Weekly, R.T., Wilcock, W.S.D., Toomey, D.R., Hooft, E.E.E., & Kim, E. (2014). Upper crustal seismic structure of the Endeavour segment, Juan de Fuca Ridge from traveltime tomography: Implications for oceanic crustal accretion. *Geochemistry, Geophysics, Geosystems*, *15*(4), 1296–1315. https://doi.org/10.1002/2013GC005159

Wessel, P., & Smith, W.H.F. (1998). New, improved version of Generic Mapping Tools released. *Eos, Transactions American Geophysical Union (79)*, 579-579. https://doi.org/10.1029/98EO00426.

Wilcock, W.S.D., Solomon, S.C., Purdy, G.M. & Toomey, D.R. (1992). The seismic attenuation structure of a fast-spreading mid-ocean ridge. *Science, 258*(5087), 1470-1474.

White, R.S., Mckenzie, D., & O'Nions, R.K. (1992). Oceanic crustal thickness from seismic measurements and rare earth element inversions. *Journal of Geophysical Research*, *97*(B13), 19683-19715.

Xu, M., Zhao, X., & Canales, J. P. (2020). Structural variability within the Kane oceanic core complex from full waveform inversion and reverse time migration of streamer data. Geophysical Research Letters, 47, e2020GL087405 https://doi.org/10.1029/2020GL087405

Zhang, J., & Toksöz, M.N. (1998). Nonlinear refraction traveltime tomography. *Geophysics, 63*, 1726–1737, doi: https://doi.org/10.1190/1.1444468.

Zhao, M., Qiu, X., Li, J., Sauter, D., Ruan, A., Chen, J., et al. (2013). Three-dimensional seismic structure of the Dragon Flag oceanic core complex at the ultraslow spreading Southwest Indian Ridge (49°39′E). *Geochemistry, Geophysics, Geosystems*, *14*(10), 4544–4563. https://doi.org/10.1002/ggge.20264

Zhou, H., & Dick, H.J.B. (2013). Thin crust as evidence for depleted mantle supporting the Marion Rise. *Nature*, *494*(7436), 195-200.